Appendix 1

Atmospheric Correction of Ocean Color Imagery in the Earth Observing System Era

by

Howard R. Gordon

Department of Physics
University of Miami
Coral Gables, FL 33124

Submitted to *Jour. Geophys. Res.*

Abstract

Sensors that can be used for the observation of ocean color in NASA's Earth Observing System era — SeaWiFS, MODIS, and MISR — have been designed with two-four times the radiometric sensitivity of the proof-of-concept ocean color instrument, CZCS. To realize an improvement in the retrieval of biologically important ocean parameters, e.g., the concentration of the photosynthetic pigment chlorophyll *a*, from this increased sensitivity, significantly better atmospheric correction than was applied to CZCS is required. Atmospheric correction improvement necessitates the inclusion of the effects of multiple scattering, which are strongly dependent on the aerosol size distribution, concentration, and absorption properties. We review the basic concepts of atmospheric correction over the oceans and provide the details of the algorithms currently being developed for SeaWiFS, MODIS, and MISR. An alternate correction algorithm that could be of significant value in the coastal zone, is described for MISR. Related issues such as the influence of aerosol vertical structure in the troposphere, polarization of the light field, sea surface roughness, and oceanic whitecaps on the sea surface are evaluated and plans for their inclusion in the algorithm are described. Unresolved issues, such as the presence of stratospheric aerosol, the appropriateness of the aerosol models used in the assessment of multiple scattering, and the identification of, and difficulties associated with the correction for, the presence of absorbing aerosols, e.g., urban pollution or mineral dust, are identified and suggestions are provided for their resolution.

1. Introduction

Following the work of Clarke, Ewing, and Lorenzen [*Clarke, Ewing and Lorenzen*, 1970] showing that the chlorophyll concentration in the surface waters of the ocean could be deduced from aircraft measurements of the spectrum of upwelling light from the sea — the "ocean color" — NASA launched the Coastal Zone Color Scanner (CZCS) on Nimbus-7 in late 1978 [*Gordon et al.*, 1980; *Hovis et al.*, 1980]. The CZCS was a proof-of-concept mission with the goal of measuring ocean color from space. It was a scanning radiometer that had four bands in the visible at 443, 520, 550, and 670 nm with bandwidths of 20 nm, one band in the near infrared (NIR) at 750 nm with a bandwidth of 100 nm, and a thermal infrared band (10.5 to 12.5 μm) to measure sea surface temperature. The four visible bands possessed high radiometric sensitivity (well over an order of magnitude higher than other visible sensors designed for earth resources at that time, e.g., the MSS sensor on the Landsat series) and were specifically designed for ocean color. The CZCS experience demonstrated the feasibility of the measurement of phytoplankton pigments, and possibly even productivity [*Morel and André*, 1991; *Platt and Sathyendranath*, 1988], on a *global* scale. This feasibility rests squarely on two observations: (1) there exists a more or less universal relationship between the color of the ocean and the phytoplankton pigment concentration for most open ocean waters; and (2) it is possible to develop algorithms to remove the interfering effects of the atmosphere and the sea surface from the imagery. In this paper we will describe the basis of the algorithm for removing the atmospheric and sea surface effects from ocean color sensors to be operating in the Earth Observing System (EOS) [*Asrar and Dozier*, 1994] era to derive the normalized water-leaving radiance in the visible. The process of deriving the normalized water-leaving radiance from imagery of the oceans is usually termed *atmospheric correction.* Three specific sensors will be considered: the sea-viewing wide-field-of-view sensor (SeaWiFS) [*Hooker et al.*, 1992]; the moderate resolution imaging spectroradiometer (MODIS) [*Salomonson et al.*, 1989]; and the multiangle imaging spectroradiometer (MISR) [*Diner et al.*, 1991].

The normalized water-leaving radiance, $[L_w]_N$, was defined by *Gordon and Clark* [1981] through

$$L_w(\lambda) = [L_w(\lambda)]_N \cos\theta_0 \exp\left[-\left(\frac{\tau_r(\lambda)}{2} + \tau_{Oz}(\lambda)\right)\left(\frac{1}{\cos\theta_0}\right)\right], \tag{1}$$

where $L_w(\lambda)$ is the radiance backscattered *out* of the water toward the zenith at a wavelength λ, $\tau_r(\lambda)$ and $\tau_{Oz}(\lambda)$ are the optical thicknesses of the atmosphere associated with molecular (Rayleigh) scattering and Ozone absorption, respectively. θ_0 is the solar zenith angle. The normalized water-leaving radiance is approximately the radiance that would exit the ocean in the absence of the atmosphere with the sun at the zenith. (This definition was motivated by the desire to remove, as much as possible, the effects of the atmosphere and the solar zenith angle from $L_w(\lambda)$; however, *Morel and Gentili* [1993] have shown that a residual dependence on θ_0 remains in $[L(\lambda)]_N$.) This quantity is used in other algorithms to derive nearly all of the SeaWiFS, MODIS, and MISR ocean products, e.g, the chlorophyll concentration. In what follows, we will abandon the use of radiance in the description of the algorithm in favor of reflectance. The reflectance ρ associated with a radiance L is defined to be $\pi L/F_0 \cos\theta_0$, where F_0 is the extraterrestrial solar irradiance, and θ_0 is the solar zenith angle, i.e., the angle between the line from the point on the sea surface under examination to the sun and the local vertical. Reflectance is favored because it may be possible to more accurately calibrate future sensors in reflectance rather than radiance. The desired normalized water-leaving radiance can easily be converted to normalized water-leaving reflectance $[\rho_w]_N$ through

$$[\rho_w]_N = \frac{\pi}{F_0}[L_w]_N, \tag{2}$$

and Eq. (1) becomes

$$\rho_w(\lambda) = [\rho_w(\lambda)]_N \exp\left[-\left(\frac{\tau_r(\lambda)}{2} + \tau_{Oz}(\lambda)\right)\left(\frac{1}{\cos\theta_0}\right)\right] \equiv [\rho_w(\lambda)]_N t(\theta_0, \lambda), \tag{3}$$

where $t(\theta_0, \lambda)$ is an approximation to the diffuse transmittance of the atmosphere (See Subsection 4.6). Thus, retrieving $[\rho_w]_N$ is equivalent to retrieving $[L_w]_N$. The factor π/F_0 in Eq. (2) is ≈ 0.017 at 443 and 550 nm.

Figures 1a and 1b provide $[\rho_w(\lambda)]_N$ at $\lambda = 443$ and 550 nm as a function of the pigment concentration (C, the sum of the concentrations of chlorophyll a and its degradation product phaeophytin a) for Case 1 waters, i.e., waters for which the optical properties are determined by the water itself along with the phytoplankton and their immediate detrital material. Figure 2 gives the algorithm used to estimate the pigment concentration from $[\rho_w(443)]_N/[\rho_w(550)]_N$. It can be well represented by

$$\log_{10} 3.33C = -1.2\log_{10} R + 0.5(\log_{10} R)^2 - 2.8(\log_{10} R)^3, \tag{4}$$

with $R = 0.5[\rho_w(443)]_N/[\rho_w(550)]_N$. Thus, the pigment concentration C is directly related to the radiance ratios. Analysis [*Gordon*, 1990] suggests that the pigment concentration can be derived from the radiance ratio with an error of $\sim \pm 20\%$. Because of relationships such a these that relate bio-optical parameters to $[\rho_w(\lambda)]_N$, the normalized water-leaving reflectance plays a central

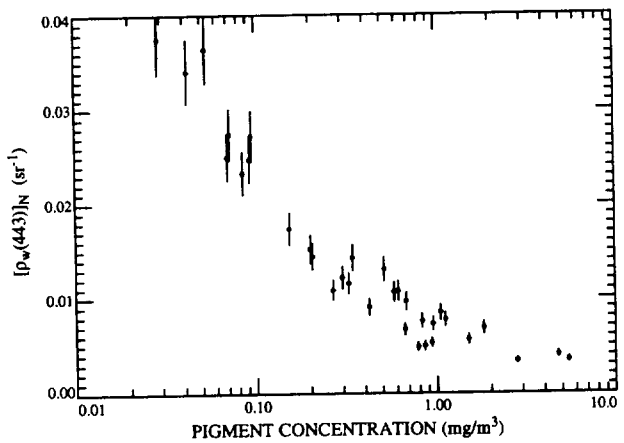

Figure 1a. Normalized water-leaving reflectance at 443 nm as a function of pigment concentration. Redrawn from *Gordon et al.* [1988].

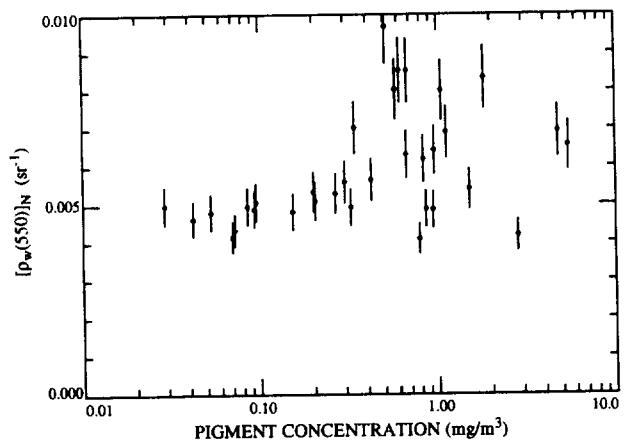

Figure 1b. Normalized water-leaving reflectance at 550 nm as a function of pigment concentration. Redrawn from *Gordon et al.* [1988].

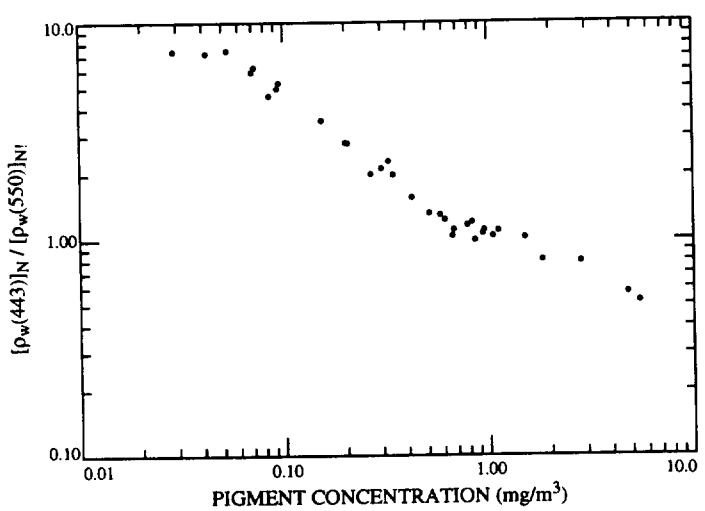

Figure 2. Normalized water-leaving reflectance ratio as a function of pigment concentration. Redrawn from *Gordon et al.* [1988].

role in the application of ocean color imagery to the oceans, and atmospheric correction becomes a critical factor in determining the fidelity with which bio-optical parameters can be retrieved.

We will begin the discussion with a basic overview of atmospheric correction, including the original CZCS algorithm and the advanced algorithm proposed for SeaWiFS (and the prototype for MODIS and MISR). Next we assess the magnitude of errors induced by the simplifying assumptions used to make the SeaWiFS algorithm tractable, and discuss several unresolved issues. Finally, we examine an alternate approach that could be employed with MISR.

Before beginning, however, a few preliminaries are useful. Table 1 provides the radiometric specification for the "ocean" bands on MODIS in terms of reflectance for a solar zenith angle of 60°. In the table, λ is the nominal band center and ρ_{max} is the radiance at which the sensor saturates. For convenience we also provide the "noise equivalent reflectance" (NE$\Delta\rho$) for the Sea-

Table 1: Radiometric performance of MODIS compared with SeaWiFS, MISR, and CZCS for $\theta_0 = 60°$.

Band	λ (nm)	ρ_{max} (Sr^{-1})	ρ_t (Sr^{-1})	$[\rho_w]_N$ (Sr^{-1})	NE$\Delta\rho$ (Sr^{-1})			
					MODIS	SeaWiFS	MISR	CZCS
8	412	0.50	0.34	0.040	0.00018	0.00068	–	–
9	443	0.46	0.29	0.038	0.00016	0.00043	0.00024	0.0011
10	490	0.36	0.23	0.024	0.00014	0.00034	–	–
11	530	0.30	0.19	0.0090	0.00013	0.00031	–	0.00058
12	550	0.25	0.154	0.0050	0.00010	0.00027	0.00020	0.00064
13	670	0.17	0.105	0.0004	0.00004	0.00023	0.00017	0.00051
14	681	0.17	0.105	0.0003	0.00004	–	–	–
15	750	0.15	0.081	–	0.000085	0.00018	–	–
16	865	0.13	0.069	–	0.000076	0.00015	0.00013	–

WiFS, MISR, and CZCS bands closest to the given MODIS band. With the exception of CZCS, the NE$\Delta\rho$ values provided are based on the individual instrument specifications, and may be significantly lower in the completed instruments. The MISR NE$\Delta\rho$ values are for a 1 km $\times$ 1 km pixel size, i.e., approximately the same size as the other sensors. Note that MODIS is typically 2-3 times more sensitive than SeaWiFS, which in turn is approximately twice as sensitive as CZCS. Exceptions are the MODIS bands 13 and 14 which are to be used to measure the chlorophyll *a* fluorescence near 683 nm [*Neville and Gower*, 1977]. These bands are $\sim$ 6 times more sensitive than SeaWiFS and $\sim$ 12 times more sensitive than CZCS. MISR is a little more sensitive than

SeaWiFS. The table also provides the typical top-of-the-atmosphere reflectance ρ_t and the normalized water-leaving reflectance $[\rho_w]_N$ for a very low pigment concentration (Sargasso Sea in summer) [*Gordon and Clark*, 1981]. Note that $[\rho_w]_N$ is only a small fraction of ρ_t. To recover $[\rho_w]_N$ in the blue (443 nm) for these waters with an error $< 5\%$ requires an atmospheric correction of $\sim \pm 0.001$ to ± 0.002 in reflectance, i.e., about five to ten times the NE$\Delta\rho$. This is our goal for MODIS band 9. It is shown later that when this goal is met, the error in $[\rho_w]_N$ at 550 nm will be $\sim$ 3–4 times smaller than that at 443 nm. In this case, Figure 1 shows that the error in the ratio R in Eq. (4) usually will be dominated by error in $[\rho_w]_N$ at 443 nm, the exception being very low values of C.

The critical bands for atmospheric correction are those with nominal band centers $\lambda > 700$ nm, i.e., bands in the near infrared (NIR). Because of the strong absorption by liquid water, virtually no light will exit the ocean in these bands, except in the most turbid coastal waters, so the measured radiance originates from the scattering of solar irradiance by the atmosphere and by the sea surface. These bands can then be used to estimate the atmospheric effects by first assessing the contribution of the atmosphere in the NIR, and then extrapolating it into the visible.

2. Atmospheric Correction

The radiance received by a sensor at the top of the atmosphere (TOA) in a spectral band centered at a wavelength λ_i, $L_t(\lambda_i)$, can be divided into the following components: $L_{path}(\lambda_i)$ the radiance generated along the optical path by scattering in the atmosphere *and* by specular reflection of atmospherically scattered light (skylight) from the sea surface; $L_g(\lambda_i)$ the contribution arising from specular reflection of direct sunlight from the sea surface (sun glitter); $L_{wc}(\lambda_i)$ the contribution arising from sunlight and skylight reflecting from individual whitecaps on the sea surface; and, $L_w(\lambda_i)$ the desired water-leaving radiance; i.e.,

$$L_t(\lambda_i) = L_{path}(\lambda_i) + T(\lambda_i)L_g(\lambda_i) + t(\lambda_i)L_{wc}(\lambda_i) + t(\lambda_i)L_w(\lambda_i). \tag{5}$$

L_{wc} and L_w are area-weighted averages of the radiance leaving whitecap-covered and whitecap-free areas of the surface, respectively. In this equation, T and t are the direct and diffuse, transmittance of the atmosphere, respectively. The diffuse transmittance is appropriate for the water-leaving radiance and the whitecap radiance as they have near-uniform angular distribution. It is

discussed in detail in Subsection 4.6. In contrast, to the diffuse transmittance, the direct transmittance is appropriate when the angular distribution of the radiance is approximately a Dirac delta function. As the sun glitter is highly directional (except at high wind speeds), its transmittance is approximated by the direct transmittance. The direct transmittance is given by

$$T(\theta_v, \lambda) = \exp\left[-\left(\tau_r(\lambda) + \tau_{Oz}(\lambda) + \tau_a(\lambda)\right)\left(\frac{1}{\mu_v}\right)\right],$$

where $\mu_v = \cos\theta_v$, θ_v is the angle the exiting radiance makes with the upward normal at the TOA, and τ_r, τ_a, and τ_{Oz} are, respectively, the Rayleigh, aerosol, and Ozone optical thicknesses. In this equation, we have ignored the possibility of weak continuum (in the atmospheric windows) absorption by water vapor [*Eldridge*, 1967; *Tomasi*, 1979a; *Tomasi*, 1979b] due to the extreme difficulty in separating the direct effect of water vapor absorption from the indirect effect that water vapor will have on the extinction of hygroscopic aerosols [*Fraser*, 1975]. Converting to reflectance Eq. (5) becomes

$$\rho_t(\lambda_i) = \rho_{path}(\lambda_i) + T(\lambda_i)\rho_g(\lambda_i) + t(\lambda_i)\rho_{wc}(\lambda_i) + t(\lambda_i)\rho_w(\lambda_i). \tag{6}$$

Thus, from the measured $\rho_t(\lambda_i)$ we require an algorithm that provides accurate estimates of $\rho_{path}(\lambda_i)$, $T(\lambda_i)\rho_g(\lambda_i)$, $t(\lambda_i)\rho_{wc}(\lambda_i)$, and $t(\lambda_i)$. Near the sun's glitter pattern $T(\lambda_i)\rho_g(\lambda_i)$ is so large that the imagery is virtually useless and must be discarded. A sun glitter mask to remove seriously contaminated pixels is described in Appendix A. Away from the glitter pattern, i.e., where values of $T(\lambda_i)\rho_g(\lambda_i)$ become negligibly small, the largest of the remaining terms, and most difficult to estimate, is $\rho_{path}(\lambda_i)$. This difficulty is principally due to the aerosol by virtue of its highly variable concentration and optical properties. Thus, we concentrate on this term first, then consider $t(\lambda_i)\rho_{wc}(\lambda_i)$ and the ancillary data required to operate the algorithm.

In general, ρ_{path} can be decomposed into several components:

$$\rho_{path} = \rho_r(\lambda) + \rho_a(\lambda) + \rho_{ra}(\lambda) \tag{7}$$

where ρ_r is the reflectance resulting from multiple scattering by air molecules (Rayleigh scattering) in the absence of aerosols, ρ_a is the reflectance resulting from multiple scattering by aerosols in the absence of the air, and ρ_{ra} is the interaction term between molecular and aerosol scattering [*Deschamps, Herman and Tanre*, 1983]. The term ρ_{ra} accounts for the interaction between Rayleigh and aerosol scattering, e.g., photons first scattered by the air then scattered by aerosols,

or photons first scattered by aerosols then air, etc. This term is zero in the single scattering case, in which photons are only scattered once, and it can be ignored as long as the amount of multiple scattering is small, i.e., at small Rayleigh and aerosol optical thicknesses. We note that given the surface atmospheric pressure (to determine the value of τ_r) and the surface wind speed (to define the roughness of the sea surface), ρ_r can be computed accurately, even accounting for polarization effects [*Gordon, Brown and Evans*, 1988; *Gordon and Wang*, 1992b].

In modeling the propagation of radiance in the ocean-atmosphere system, we assume that the atmosphere can be considered to be a vertically stratified, plane parallel medium. The medium is described by providing the extinction coefficient, $c(h)$, as a function of altitude h, the scattering phase function for scattering of radiance from direction $\hat{\xi}'$ to direction $\hat{\xi}$, $P(h;\hat{\xi}' \rightarrow \hat{\xi})$, and the single scattering albedo $\omega_0(h)$. Replacing h by the optical depth τ defined as

$$\tau(h) = \int_h^\infty c(h)\, dh,$$

the propagation of radiance in such a medium in the scalar approximation (the polarization state of the radiance and the change in polarization induced by the scattering process is ignored) is governed by the radiative transfer equation (RTE):

$$\hat{\xi} \bullet \hat{n} \frac{dL(\tau,\hat{\xi})}{d\tau} = -L(\tau,\hat{\xi}) + \frac{\omega_0(\tau)}{4\pi} \int_{\text{all } \hat{\xi}'} P(\tau;\hat{\xi}' \rightarrow \hat{\xi}) L(\tau,\hat{\xi}')\, d\Omega(\hat{\xi}'),$$

where $d\Omega(\hat{\xi}')$ is the differential of solid angle around the direction $\hat{\xi}'$, and $\hat{n}$ is a unit vector in the nadir direction (normal to the sea surface pointed down). Analytical solutions to the RTE are possible only in the simplest case, e.g., $\omega_0 = 0$, so normally one must be satisfied with numerical solutions.

In principal this equation must be solved for the coupled ocean-atmosphere system; however, because of the very low albedo of the ocean (Table 1) it is not necessary to consider the coupling [*Gordon*, 1976], i.e., we can ignore processes such as photons being backscattered out of the water and then scattered back into the water and backscattered out again, etc. The water-leaving radiance simply propagates to the sensor (ρ_{path} is independent of ρ_w in Eq. (6)) and the ocean and atmosphere decouple, hence, we need only understand the solution of the atmospheric part of the problem, i.e., an atmosphere bounded by a Fresnel-reflecting ocean surface.

As the goal of atmospheric correction is to retrieve $\rho_w(443)$ with an uncertainty less than ± 0.002, i.e., $\sim \pm 0.6\%$ of $\rho_t(443)$ (Table 1), for the development and testing of the algorithm we

require solutions of the RTE that yield ρ_t with an uncertainty $\ll 0.6\%$. For the bulk of the work described here, ρ_t was generated using the successive-order-of-scattering method [*van de Hulst*, 1980]. To understand the accuracy of this code, a second code was developed employing Monte Carlo methods. Typically, the values of ρ_t produced by the two codes differ by less than 0.05%. Thus, either code could meet the accuracy required for this work.

We will assume, as justified earlier, that $\rho_w = 0$ in the NIR. The problem we are required to solve can then be stated in a simple manner: given the satellite measurement of the radiance (reflectance) of the ocean-atmosphere system in the NIR, predict the radiance (reflectance) that would be observed in the visible. The difference between the predicted and the measured radiance (reflectance) of the ocean-atmosphere system is the water-leaving radiance (reflectance) transmitted to the top of the atmosphere.

2.1 Single scattering

It is useful to consider $\rho_{path}(\lambda_i)$ in the the limit that the optical thickness of the atmosphere is $\ll 1$. We refer to this as the single-scattering limit. Formulas for the reflectances in this limit are referred to as the single-scattering approximation. The CZCS algorithm was based on the single-scattering approximation. In this approximation the path reflectance reduces to

$$\rho_{path}(\lambda_i) = \rho_r(\lambda_i) + \rho_{as}(\lambda_i), \tag{8}$$

with the aerosol contribution ρ_{as} provided by

$$\rho_{as}(\lambda) = \omega_a(\lambda)\tau_a(\lambda)p_a(\theta_v, \phi_v; \theta_0, \phi_0; \lambda)/4\cos\theta_v\cos\theta_0, \tag{9}$$

$$p_a(\theta_v, \phi_v; \theta_0, \phi_0; \lambda) = P_a(\theta_-, \lambda) + \Big(r(\theta_v) + r(\theta_0)\Big)P_a(\theta_+, \lambda),$$

$$\cos\theta_\pm = \pm\cos\theta_0\cos\theta_v - \sin\theta_0\sin\theta_v\cos(\phi_v - \phi_0),$$

where $P_a(\alpha, \lambda)$ is the aerosol scattering phase function for a scattering angle α, ω_a is the aerosol single scattering albedo, and $r(\alpha)$ is the Fresnel reflectance of the interface for an incident angle α. The angles θ_0 and ϕ_0 are, respectively, the zenith and azimuth angles of a vector from the point on the sea surface under examination (pixel) to the sun, and likewise, θ_v and ϕ_v are the zenith and azimuth angles of a vector from the pixel to the sensor. These are measured with respect to the *upward* normal so θ_v and θ_0 are both less than 90° in these equations. In what follows usually we take $\phi_0 = 0$.

We assume we are given the the path reflectance at two bands in the NIR at λ_s and λ_l, where the subscript "s" stands for short and "l" for long, e.g., for MODIS $\lambda_s = 750$ nm and $\lambda_l = 865$ nm, for SeaWiFS $\lambda_s = 765$ and $\lambda_l = 865$, for MISR $\lambda_s = 670$ nm and $\lambda_l = 865$ nm, while for CZCS there were no NIR bands. This would be accomplished in the following manner. We ignore sun glitter, i.e., assume θ_v is outside the glitter pattern, and assume that $t(\lambda_i)\rho_{wc}(\lambda_i)$ has been provided, then, since we can take $\rho_w = 0$ at both λ_s and λ_l, ρ_{path} can be estimated from the measured ρ_t at both λ_s and λ_l. As $\rho_r(\lambda)$ can be computed accurately, $\rho_{as}(\lambda_s)$ and $\rho_{as}(\lambda_l)$ are determined from the associated values of ρ_{path} at λ_s and λ_l. This allows estimation of the parameter $\varepsilon(\lambda_s, \lambda_l)$:

$$\varepsilon(\lambda_s, \lambda_l) \equiv \frac{\rho_{as}(\lambda_s)}{\rho_{as}(\lambda_l)} = \frac{\omega_a(\lambda_s)\tau_a(\lambda_s)p_a(\theta_v, \phi_v; \theta_0, \phi_0; \lambda_s)}{\omega_a(\lambda_l)\tau_a(\lambda_l)p_a(\theta_v, \phi_v; \theta_0, \phi_0; \lambda_l)}. \tag{10}$$

If we can compute the value of $\varepsilon(\lambda_i, \lambda_l)$ for the band at λ_i from the value of $\varepsilon(\lambda_s, \lambda_l)$, this will yield $\rho_{as}(\lambda_i)$, which, when combined with $\rho_r(\lambda_i)$, provides the desired $\rho_{path}(\lambda_i)$:

$$\rho_{path}(\lambda_i) = \rho_r(\lambda_i) + \varepsilon(\lambda_i, \lambda_l)\rho_{as}(\lambda_l). \tag{11}$$

Clearly, the key to utilizing this procedure is the estimation of $\varepsilon(\lambda_i, \lambda_l)$ from $\varepsilon(\lambda_s, \lambda_l)$.

2.1.1 The CZCS algorithm

The atmospheric correction algorithm for CZCS was described in detail in *Evans and Gordon* [1994]. Briefly, the basic CZCS algorithm [*Gordon*, 1978; *Gordon and Clark*, 1980] was based on single scattering; however, $\rho_r(\lambda_i)$ was computed accurately, including the effects of multiple scattering and polarization [*Gordon, Brown and Evans*, 1988]. As there were no NIR bands, the algorithm could not be operated as described in Section 2.1. However, Table 1 shows that $\rho_w(670)$ can generally be taken to be zero (at least if the pigment concentration is low enough). Thus, the single scattering algorithm was typically operated with $\lambda_l = 670$ nm and $\rho_w(\lambda_l) = 0$. Unfortunately, there was no shorter wavelength (λ_s) for which $\rho_w = 0$, so in the processing of the CZCS global data set [*Feldman et al.*, 1989] $\varepsilon(\lambda_i, \lambda_s)$ was set equal to unity. This is characteristic of a maritime aerosol at high relative humidity (Subsection 2.1.2).

For sufficiently low C values, Figure 1b suggests that $[L_w(550)]_N$, and hence $[\rho_w(550)]_N$ is approximately constant. This fact can be used to estimate $\varepsilon(550, 670)$ for such "clear water" regions [*Gordon and Clark*, 1981] in a scene, allowing a basis for extrapolation to 520 and 443 nm.

If the resulting $\varepsilon(\lambda_i, \lambda_l)$ is then assumed to be valid for the entire image, retrieval of $[\rho_w(\lambda_i)]_N$ and C can be effected for the image. This is the procedure used by *Gordon et al.* [1983] in the Middle Atlantic Bight. Unfortunately, there are serious difficulties applying this procedure routinely. For example, the image of interest may contain no "clear water," the ε's may vary over the image because of variations in aerosol type [*André and Morel*, 1991; *Bricaud and Morel*, 1987], and the pigment concentration may not be small enough to take $\rho_w = 0$ at 670 nm. Morel and his co-workers have developed a promising approach for dealing these problems in Case 1 waters [*André and Morel*, 1991; *Bricaud and Morel*, 1987] based on the ideas of *Smith and Wilson* [1981]. This involves utilizing a modeled relationship between C and $[\rho_w(\lambda_i)]_N$. Fortunately, for the sensors of concern in this paper (SeaWiFS, MODIS, and MISR), these problems are circumvented by virtue of the additional spectral band(s) with $\lambda > 700$ nm.

2.1.2 Application to EOS era sensors

As the key extrapolation to $\varepsilon(\lambda_i, \lambda_l)$ from $\varepsilon(\lambda_s, \lambda_l)$ for application of the single scattering algorithm to the EOS era sensors involves more than a factor of two in wavelength, it is important to try to gain some insight into the possible spectral behavior of $\varepsilon(\lambda_i, \lambda_l)$. This has been attempted by *Gordon and Wang* [1994a] by computing $\varepsilon(\lambda_i, \lambda_l)$ for several aerosol models. Briefly, they used aerosol models that were developed by *Shettle and Fenn* [1979] for LOWTRAN-6 [*Kenizys et al.*, 1983]. These models consist of particles distributed in size according to combinations of log-normal distributions. The size frequency distribution $n(D)$ is given by

$$n(D) = \sum_{i=1}^{2} n_i(D),$$

with

$$n_i(D) = \frac{dN_i(D)}{dD} = \frac{N_i}{\log_e(10)\sqrt{2\pi}\sigma_i D} \exp\left[-\frac{1}{2}\left(\frac{\log_{10}(D/D_i)}{\sigma_i}\right)^2\right],$$

where, $dN_i(D)$ is the number of particles per unit volume between D and $D + dD$, D_i and σ_i are the median diameter and the standard deviation, respectively, and N_i is the total number density of the ith component. Since hygroscopic particles swell with increasing relative humidity (RH), D_i and σ_i are functions of RH. The smaller size fraction is a mixture of 70% water soluble and 30% dust-like particles called the Tropospheric aerosol. It has been used to represent the aerosols within the free troposphere above the boundary-layer [*Shettle and Fenn*, 1979]. The refractive index m for this component at 550 nm ranges from $1.53 - 0.0066i$ at RH = 0, to

$1.369 - 0.0012i$ at RH = 98%. Thus as the particles absorb more water, the real part of their refractive index approaches that of water and the imaginary part (proportional to the absorption coefficient) decreases. Because of the moderate imaginary part of the refractive index, these particles have weak absorption and ω_a ranges from 0.959 to 0.989 for $0 \leq$ RH $\leq$ 98%. The modal diameter of this component is always < 0.1 μm. The larger fraction is a sea salt-based component, the "Oceanic" aerosol. Its modal diameter varies from about 0.3 to 1.2 μm as RH varies from 0 to 98%. Its index of refraction is essentially real (imaginary part $\sim 10^{-8}$), so $\omega_a = 1$. Like the tropospheric aerosol its real part ranges from 1.5 at RH = 0 to 1.35 at RH = 98%.

From these components, three basic models were constructed: the Tropospheric model with no Oceanic contribution; the Maritime model for which 99% of the particles have the Tropospheric characteristics and 1% the Oceanic; and the Coastal model for which 99.5% of the particles have the Tropospheric characteristics and 0.5% the Oceanic. *Gordon and Wang* [1994a]

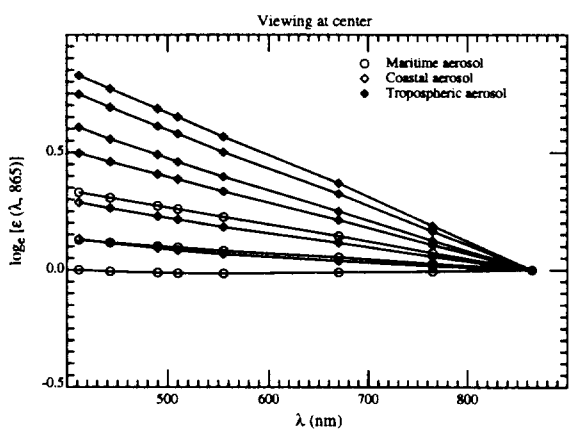

Figure 3a. $\varepsilon(\lambda, 865)$ for nadir viewing with $\theta_0 = 60°$ for the Maritime, Coastal, and Tropospheric aerosol models. For each model, the RH values are 50, 80, and 98% from the upper to the lower curves.

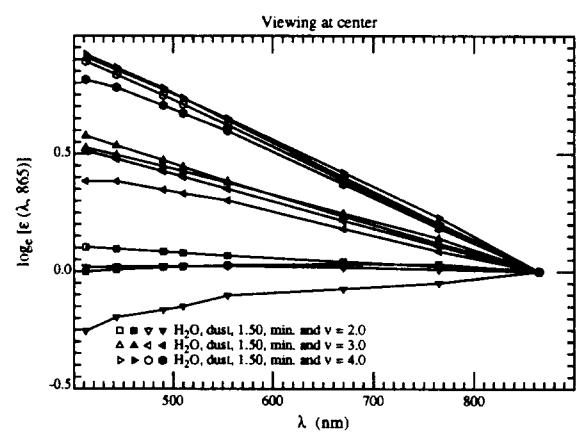

Figure 3b. $\varepsilon(\lambda, 865)$ for nadir viewing with $\theta_0 = 60°$ for the Haze C models. Note that the open symbols are for models with little or no absorption, while the filled symbols are for absorbing models.

introduced the Coastal aerosol model to represent the aerosol over the oceans nearer the coast (less Oceanic contribution). The properties of all three aerosol models depend on the wavelength and relative humidity. With the values of D_i, σ_i, and $m_i(\lambda)$ taken from *Shettle and Fenn* [1979], Mie theory was used to calculate the optical properties for all three models for the SeaWiFS–MODIS–MISR spectral bands at different relative humidities.

Sample results for $\varepsilon(\lambda_i, \lambda_l)$, where λ_l is taken to be 865 nm (SeaWiFS), are presented in Figure 3a. These computations suggest that there should be a strong variation of ε with aerosol model and RH. The increase in particle size (due to swelling) with increasing RH clearly reduces the spectral variation of ε. The spectral variation of ε is due in large part to the spectral variation of the aerosol optical thickness, τ_a; however, additional variation is produced by the aerosol phase function. Note that Figure 3a is plotted in a format that would yield a straight line under the hypothesis that $\varepsilon(\lambda_i, \lambda_l) = \exp\left[c(\lambda_l - \lambda_i)\right]$, where c is a constant. This shows that over the range 412–865 nm $\varepsilon(\lambda_i, \lambda_l)$ can be considered to be an exponential function of $\lambda_l - \lambda_i$, for the *Shettle and Fenn* [1979] models. *Wang and Gordon* [1994b] have used this fact to extend the CZCS algorithm for use with SeaWiFS and MODIS.

We now examine the accuracy of this CZCS-type single-scattering algorithm based on an assumed exponential spectral variation of $\varepsilon(\lambda_i, \lambda_l)$. For this purpose, we simulated atmospheres using an array of aerosol models. First, the aerosol optical properties were taken from the Tropospheric, Coastal, and Maritime models at RH = 80%, denoted, respectively, as T80, C80, and M80. Then, we simulated the aerosol using the *Shettle and Fenn* [1979] Urban model at RH = 80% (U80). This model shows strong absorption. In addition to the water soluble and dust-like particles of the Tropospheric model, the Urban model contains soot-like particles (combustion products). Also, the Urban model has a second, larger particle, mode in addition to that of the Tropospheric model. At 865 nm the Mie theory computations yielded, $\omega_a = 0.9934$, 0.9884, and 0.9528, respectively, for the Maritime, Coastal, and Tropospheric models (RH = 80%), while in contrast, $\omega_a = 0.7481$ for the Urban model. Here, the Urban model is intended to represent aerosols that might be present over the oceans near areas with considerable urban pollution, e.g., the Middle Atlantic Bight off the U.S. East Coast in summer. Finally, we examined aerosols with a different analytical form for the size distribution [*Junge*, 1958]:

$$
\begin{aligned}
n(D) = \frac{dN(D)}{dD} &= K, & D_0 < D < D_1, \\
&= K\left(\frac{D_1}{D}\right)^{\nu+1}, & D_1 < D < D_2, \\
&= 0, & D > D_2,
\end{aligned}
$$

with $D_0 = 0.06\ \mu$m, $D_1 = 0.20\ \mu$m, and $D_2 = 20\ \mu$m. Following *Deirmendjian* [1969] we call these Haze C models. Twelve separate models were considered: $\nu = 2$, 3, and 4, with the refractive index of the particles taken to be that of liquid water (from *Hale and Querry* [1973]), close to that of the dust component in the Tropospheric model ($1.53 - 0.008i$), nonabsorbing crystals

$(1.50 - 0i)$, and absorbing minerals that might be expected from desert aerosols transported over the oceans [*d'Almeida, Koepke and Shettle*, 1991]. The spectral behavior of $\varepsilon(\lambda, 865)$ for these models is presented in Figure 3b. We see that the absorption-free (open symbols) Haze C models display a behavior similar to the Shettle and Fenn models; however, for models with strong absorption (solid symbols) departures are seen, especially for the mineral models for which the imaginary part of the refractive index increases with decreasing λ.

Using these aerosol models we generated hypothetical atmospheres with a two-layer structure: the aerosols occupying the lower layer, and all molecular scattering confined to the upper layer. This distribution of aerosols is similar to that typically found over the oceans when the aerosol is locally generated, i.e., most of the aerosol is confined to the marine boundary layer [*Sasano and Browell*, 1989]. The atmosphere was bounded by a flat (smooth) Fresnel-reflecting sea surface, and all photons that penetrate the interface are assumed to be absorbed in the ocean. The RTE in the scalar approximation was solved for this hypothetical atmosphere using the successive-

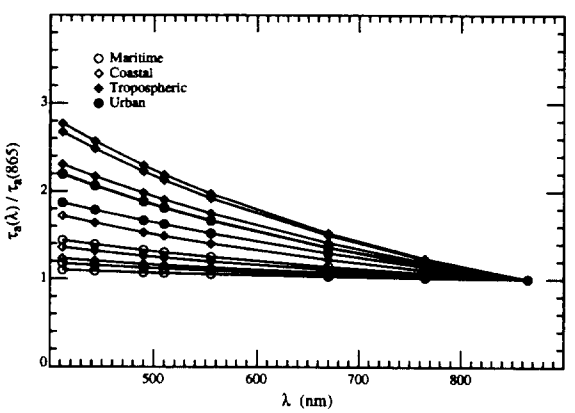

Figure 4a. Spectral variation of τ_a for the Maritime, Coastal, and Tropospheric aerosol models. For each model, the RH values are 50, 80, and 98% from the upper to the lower curves.

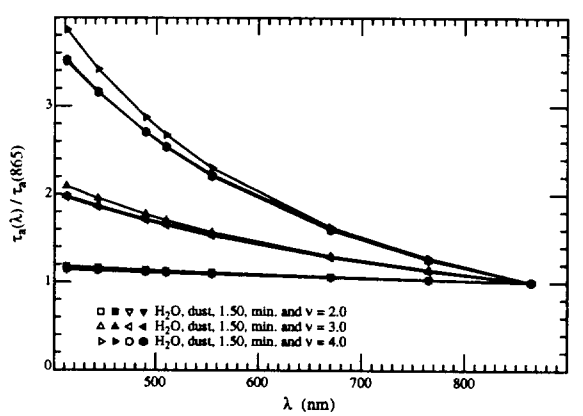

Figure 4b. Spectral variation of τ_a for the Haze C models. Note that the open symbols are for models with little or no absorption, while the filled symbols are for absorbing models.

order-of-scattering method [*van de Hulst*, 1980] to provide pseudo TOA reflectance (ρ_t) data. All significant orders of multiple scattering were included. As the surface was assumed to be smooth (no wind), the sun glitter and whitecap terms in Eq. (6) are absent. The simulations of ρ_t were carried out for the following geometries: $\theta_0 = 20°$, $40°$, and $60°$, with $\theta_v \approx 1°$ and $\phi_v - \phi_0 = 90°$, i.e., viewing near the MODIS scan center: and $\theta_0 = 0°$, $20°$, $40°$, and $60°$, with $\theta_v \approx 45°$ and

$\phi_v - \phi_0 = 90°$, i.e., viewing near the scan edge. In this manner a wide range of sun-viewing geometries were included. Four wavelengths were considered: $\lambda_i = 443$, 555, 765, and 865 nm. The values used for the aerosol optical thickness at 865 nm, $\tau_a(865)$, were 0.1, 0.2, 0.3, and 0.4. The values of $\tau_a(\lambda_i)$ at the other wavelengths were determined from the spectral variation of the extinction coefficient for each particular model. These are provided in Figure 4. The Haze C models clearly show that the spectral variation of τ_a is principally determined by the size distribution, with the index of refraction playing only a minor role. Equation (10) suggests that there should be a relationship between $\tau_a(\lambda)/\tau_a(865)$ and $\varepsilon(\lambda, 865)$. Figure 5 provides an example of this for $\theta_0 = 60°$ and nadir viewing, i.e., the same geometry as in Figure 3, with $\varepsilon(765, 865)$ used rather than $\varepsilon(443, 865)$. Thus, for a given $\tau_a(865)$, $\tau_a(443)$ will generally increase with increasing $\varepsilon(765, 865)$. This will be useful in interpreting the results described below.

As the true $\rho_w(\lambda_i)$ is taken to be zero in the pseudo data (all photons entering the water are absorbed), the error in atmospheric correction, i.e., the error in the retrieved water-leaving

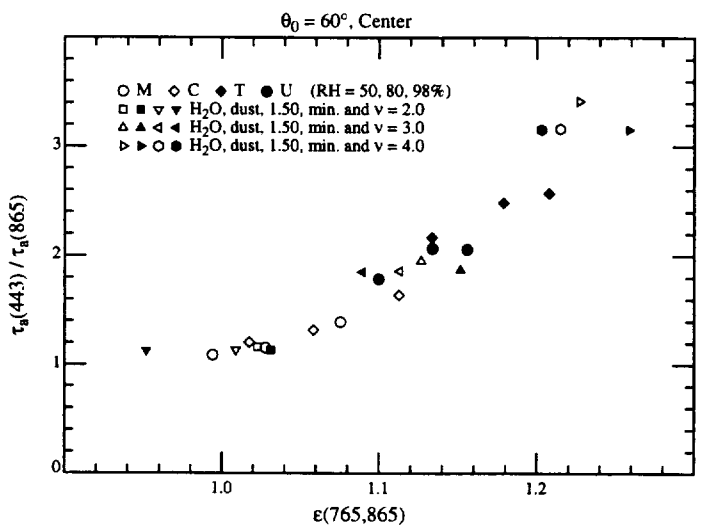

Figure 5. Relationship between $\varepsilon(765, 865)$ and $\tau_a(443)/\tau_a(865)$ for the various aerosol models with $\theta_0 = 60°$ and nadir viewing.

reflectance, $\Delta(t\rho_w)$, is just the error in the predicted path radiance. This is

$$\Delta\big(t\rho_w(\lambda_i)\big) = \rho_t(\lambda_i) - \rho_{path}(\lambda_i) = \rho_t(\lambda_i) - \rho_r(\lambda_i) - \varepsilon^{(e)}(\lambda_i, \lambda_l)\rho_{as}(\lambda_l), \tag{12}$$

where $\varepsilon^{(e)}(\lambda_i, \lambda_l)$ is the estimated value of $\varepsilon(\lambda_i, \lambda_l)$ assuming an exponential variation with λ_i:

$$\varepsilon^{(e)}(\lambda_i, \lambda_l) \equiv \exp[c(\lambda_l - \lambda_i)] = \exp\left[\left(\frac{\lambda_l - \lambda_i}{\lambda_l - \lambda_s}\right) \log_e \left(\frac{\rho_{as}(\lambda_s)}{\rho_{as}(\lambda_l)}\right)\right].$$

$\rho_r(\lambda_i)$ was computed using the same radiative transfer code, i.e., it includes all effects of multiple scattering, but not polarization. In an actual application, $\rho_r(\lambda_i)$ would be computed using a code that included polarization as well [*Gordon, Brown and Evans*, 1988]. Figure 6 provides the error in the retrieved normalized water-leaving reflectance, $\Delta[\rho_w(443)]_N$, for the seven sun-viewing geometries and for $\tau_a(865) = 0.1$ and 0.2. To derive $\Delta[\rho_w]_N$ from $\Delta t \rho_w$, the approximation for t in Eq. (3) was utilized (see Subsection 4.6). The x-axis in Figure 6, $\varepsilon^{(e)}(765, 865)$, is the *estimated* value for the indicated model and geometry.

In the absence of aerosol absorption (open symbols), the performance of this simple algorithm is truly remarkable, as Figures 4b and 5 show that for $\nu = 4$, $\tau_a(443) \approx 0.35$ and 0.70 for Figures 6a and 6b, respectively. The large negative errors for $\nu = 4$ occur at the scan edge with $\theta_0 = 60°$, i.e., the geometry with the most multiple scattering. For $\nu = 3$ ($\tau_a(443) \sim 0.2$ and 0.4 (Figures 4b and 5 for Figures 6a and 6b, respectively), the retrieved value of $[\rho_w(443)]_N$ is usually within the acceptable limits.

In the case of absorbing aerosols, the errors are seen to be mostly negative, and to grow rapidly with $\tau_a(443)$. Negative errors are particularly troublesome as they can lead to negative

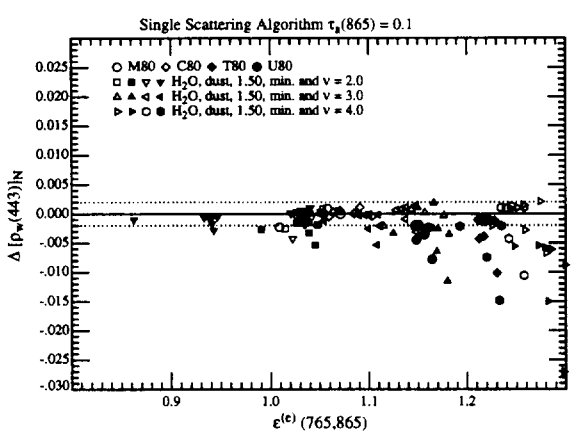

Figure 6a. $\Delta[\rho_w(443)]_N$ as a function of $\varepsilon^{(e)}(765, 865)$ for $\tau_a(865) = 0.1$ and all of the aerosol models and viewing geometries examined in the study.

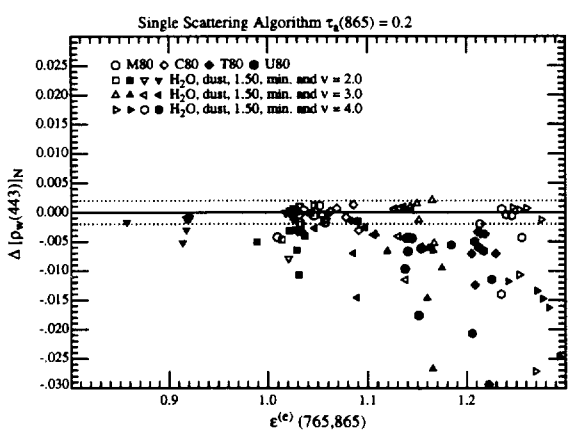

Figure 6b. $\Delta[\rho_w(443)]_N$ as a function of $\varepsilon^{(e)}(765, 865)$ for $\tau_a(865) = 0.2$ and all of the aerosol models and viewing geometries examined in the study.

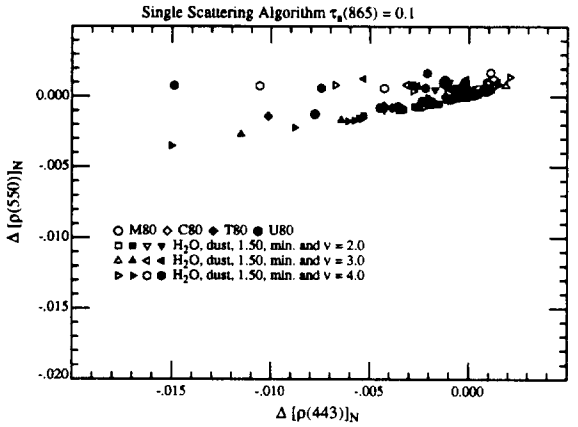

Figure 6c. $\Delta[\rho_w(550)]_N$ as a function of $\Delta[\rho_w(443)]_N$ for the results in Figure 6a.

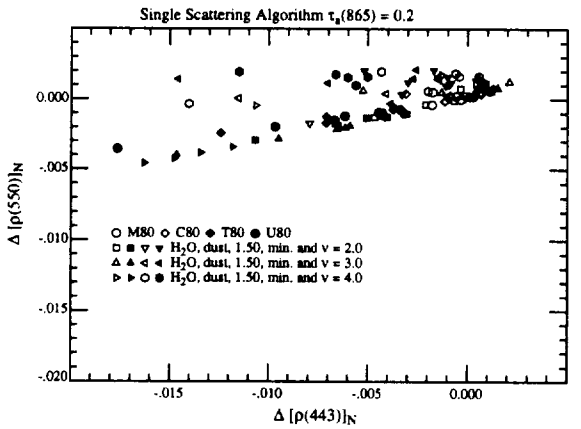

Figure 6d. $\Delta[\rho_w(550)]_N$ as a function of $\Delta[\rho_w(443)]_N$ for the results in Figure 6b.

values in the retrieved $[\rho_w(443)]_N$ when the pigment concentration $\gtrsim 0.5 - 1.0$ mg/m^3. The source of the error for absorbing aerosols is twofold. For the Haze C aerosol, it can be seen from Figure 3b that, in contrast to the nonabsorbing aerosols, an exponential extrapolation of $\varepsilon(765, 865)$ to $\varepsilon(443, 865)$ would lead to an erroneous overestimation of $\varepsilon(443, 865)$, the single exception being the mineral aerosol with $\nu = 2$. This will cause an overestimation of the aerosol contribution at 443 nm, which in turn will result in a negative error in $[\rho_w(443)]_N$. In contrast, the extrapolation does work well for T80 (Figure 3a) and, as we shall see later, in this case the error is principally due to multiple scattering, which is strongly influenced by even weak absorption.

The error in $[\rho_w(550)]_N$ as related to the associated error in $[\rho_w(443)]_N$ is provided in Figures 6c and 6d. The observed improvement in atmospheric correction at 550 compared to 443 nm can be traced to the facts that (1) the ε determination requires a smaller extrapolation at 550 nm, and (2) there is less multiple scattering at 550 nm as both τ_a (Figure 4) and τ_r are smaller. Notably, the error at 550 nm is usually much less than that at 443 nm, there being a tendency for $\Delta[\rho_w(550)]_N \sim (1/4)\Delta[\rho_w(443)]_N$, although occasionally $|\Delta[\rho_w(550)]_N| \gtrsim |\Delta[\rho_w(443)]_N|$. Thus, in a pigment ratio algorithm such as Eq. (4), the error at 443 nm will usually be the more significant error in R.

It is useful at this point to review the sparse direct observations of the aerosol optical thickness over the oceans. In the open ocean, far from sources of pollution and/or sources of desert aerosols, the atmosphere is very clear. In the Pacific $\tau_a(550)$ is found in the range 0.04 to 0.24

with a mean of 0.13 and Angstrom exponent of 0.56 [*Villevalde et al.*, 1994], suggesting a mean $\tau_a(865)$ of $\sim$ 0.1 and a maximum of $\sim$ 0.19. Similar results are obtained for the North Atlantic [*Korotaev et al.*, 1993; *Reddy et al.*, 1990]. In such a region, *Lechner et al.* [1989] found that there were low concentrations of aerosol in the free troposphere possessing a Haze C-like distribution with an average ν of $\sim$ 3.5, while in the marine boundary layer the concentration was much higher (an highly variable) with an average ν of $\sim$ 1.8, and sometimes even a bimodal size distribution (the large mode presumably resulting from local generation of aerosols by breaking waves). In contrast, in the region of the Atlantic off West Africa subject to Saharan dust, *Reddy et al.* [1990] found a mean $\tau_a(550)$ of 0.4 with $\tau_a(865) \approx 0.3$, in agreement with the observations of *Korotaev et al.* [1993], $\tau_a(550) \sim 0.3$ to 0.5. In areas subject to urban pollution, even higher optical thicknesses are observed, e.g., *Reddy et al.* [1990] found a mean $\tau_a(550) \approx 0.5$ and $\tau_a(865) \approx 0.3$ in the Western North Atlantic in summer when trajectory analysis suggested the origin of the air mass was the North American continent.

Thus, direct observation suggests that over the open ocean most of the aerosol is in the marine boundary layer and, for mean conditions $\tau_a(865) \approx 0.1$. Furthermore, the size distribution is either similar to Haze C with $\nu \approx 2.5$ or bimodal like M80 or C80. Such aerosols would have $\varepsilon(765, 865) < 1.1$ (Figure 5). Figure 6a (open symbols) with $\varepsilon(765, 865) < 1.1$ is appropriate to these mean conditions and shows that the single scattering CZCS-type algorithm should be capable of retrieving $[\rho_w(443)]_N$ with the desired accuracy. For the maximum $\tau_a(865)$ ($\sim$ 0.19), Figure 6b is appropriate and under the same conditions for maximum end of the observed $\tau_a(865)$ range, and for most of the geometries good retrievals are obtained, although in some cases, the error is outside the acceptable range.

For situations with a strong continental influence, e.g., Saharan dust or urban pollution carried over the oceans by the wind, the aerosol is likely to be at least moderately absorbing. Also, $\tau_a(\lambda)$ will be sufficiently large that aerosol single scattering will no longer be an adequate approximation. Thus, we are forced to consider a full multiple scattering approach.

2.2 Multiple scattering

Multiple scattering effects have already been shown [*Deschamps, Herman and Tanre*, 1983; *Gordon, Brown and Evans*, 1988; *Gordon and Castaño*, 1987] to be significant at the level of ac-

curacy required for SeaWiFS and MODIS, i.e., $\Delta[\rho_w(443)]_N \approx 0.001 - 0.002$. Although the single scattering approach is seen to work well only for sufficiently small optical depth (Figure 6) and nonabsorbing aerosols, typically the case over the open ocean, we desire an algorithm that can cope with even extreme situations. To begin the study of the effects of multiple scattering, we examine the properties of the solutions to the RTE used in providing the pseudo data for Figure 6. Since we are ignoring sun glitter and whitecaps for the moment, we can assess the multiple scattering effects by noting that

$$\rho_t - \rho_r - t\rho_w = \rho_a + \rho_{ra} \overset{\text{Single Scattering}}{\longrightarrow} \rho_{as}.$$

Thus, comparison of $\rho_t - \rho_r - t\rho_w$ and ρ_{as} provides a direct assessment of multiple scattering. Figures 7a and 7b provide such a comparison for the Tropospheric model with RH = 50%

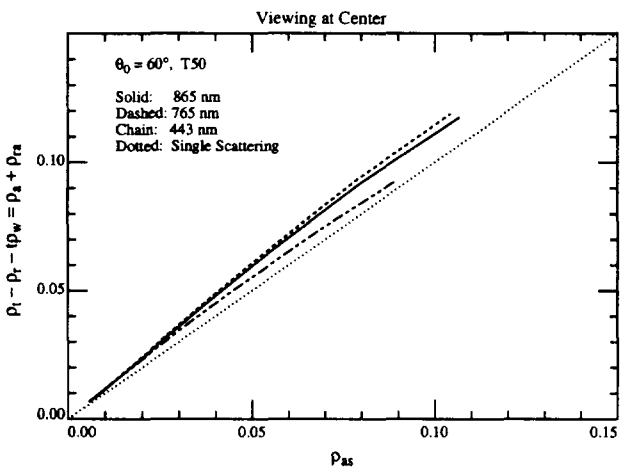

Figure 7a. $\rho_a(\lambda) + \rho_{ra}(\lambda)$ as a function of $\rho_{as}(\lambda)$ for aerosol model T50 at $\theta_0 = 60°$ and nadir viewing.

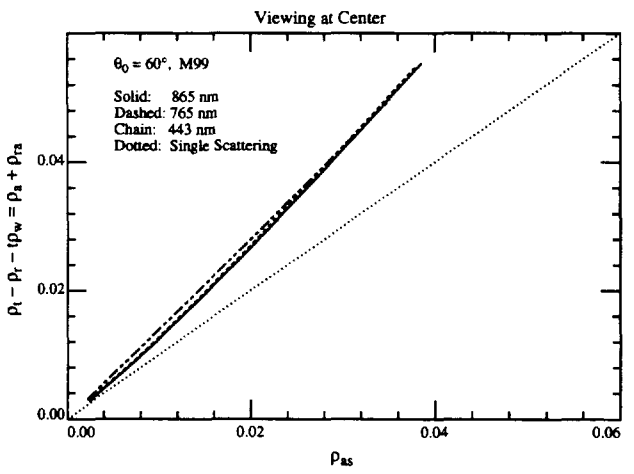

Figure 7b. $\rho_a(\lambda) + \rho_{ra}(\lambda)$ as a function of $\rho_{as}(\lambda)$ for aerosol model M99 at $\theta_0 = 60°$ and nadir viewing.

(T50) and the Maritime model with RH = 99% (M99). Note that for the Maritime aerosol for $\rho_{as} \gtrsim 0.01$, the value of $\rho_a + \rho_{ra}$ is about 40% greater that ρ_{as}, i.e., multiple scattering significantly increases the reflectance due to the aerosol. In contrast, for the Tropospheric model at RH = 50% the aerosol reflectance is only increased by $\sim$ 10%. Thus, we see that the influence of multiple scattering depends significantly on the aerosol model. In contrast to the algorithm in Subsection 2.1.2, for which multiple scattering was ignored, and for which no knowledge of the aerosol properties was required to effect the atmospheric correction, the model-dependent multiple scattering will make it necessary to utilize aerosol models in the ρ_w retrieval algorithm. As the only *direct* link to the aerosol models is through $\varepsilon(\lambda, \lambda_l)$, or in particular through $\varepsilon(\lambda_s, \lambda_l)$, it

seems reasonable to retain the formalism of the single scattering algorithm, but modify it to include multiple scattering. Writing

$$\rho_a(\lambda) + \rho_{ra}(\lambda) = K[\lambda, \rho_{as}(\lambda)]\rho_{as}(\lambda),$$

where the dependence of K on $\rho_{as}(\lambda)$ represents the departure of the $\rho_a(\lambda)+\rho_{ra}(\lambda)$ versus $\rho_{as}(\lambda)$ relationship from linearity, we see that K is nearly the same for the two NIR bands, but can be significantly different at 443 nm (Figure 7a). It is irrelevant whether the dependence of K on λ is explicit ($K = K[\lambda]$) or implicit ($K = K[\rho_{as}(\lambda)]$) or both, the effect is the same: Eq. (12) becomes

$$\Delta\big(t\rho_w(\lambda_i)\big) = \rho_t(\lambda_i) - \rho_r(\lambda_i) - \frac{K[\lambda_i, \rho_{as}(\lambda_i)]}{K[\lambda_l, \rho_{as}(\lambda_l)]}\varepsilon(\lambda_i, \lambda_l)\big[\rho_a(\lambda_l) + \rho_{ra}(\lambda_l)\big],$$

and the $\rho_a(\lambda) + \rho_{ra}(\lambda)$ versus $\rho_{as}(\lambda)$ relationship must be known at each wavelength.

The approach taken by *Gordon and Wang* [1994a] was to solve the RTE for a set of N candidate aerosol models to provide what is essentially a set of lookup tables for $K[\lambda, \rho_{as}(\lambda)]$. As in the single scattering algorithm, the NIR bands are used to provide the aerosol model through

$$\varepsilon(\lambda_s, \lambda_l) = \frac{K[\lambda_l, \rho_{as}(\lambda_l)]}{K[\lambda_s, \rho_{as}(\lambda_s)]}\left[\frac{\rho_a(\lambda_s) + \rho_{ra}(\lambda_s)}{\rho_a(\lambda_l) + \rho_{ra}(\lambda_l)}\right];$$

however, since the aerosol model is not known at this point, the K ratio is unknown. Figure 7 suggests that this K ratio should not deviate significantly from unity, so *Gordon and Wang* [1994a] proposed computing $\varepsilon(\lambda_s, \lambda_l)$ though

$$\varepsilon(\lambda_s, \lambda_l) = \frac{1}{N}\sum_{j=1}^{N} \varepsilon_j(\lambda_s, \lambda_l),$$

where $\varepsilon_j(\lambda_s, \lambda_l)$ is the value of $\varepsilon(\lambda_s, \lambda_l)$ derived from $\rho_a(\lambda_l) + \rho_{ra}(\lambda_l)$ and $\rho_a(\lambda_s) + \rho_{ra}(\lambda_s)$ by assuming that the K ratio for the jth aerosol model is correct. This procedure works reasonably well because the values of ε_j derived using the individual models are all close to the correct value. The procedure has been further modified by recomputing a new average formed by dropping the two models with the largest values of $\varepsilon(\lambda_s, \lambda_l) - \varepsilon_j(\lambda_s, \lambda_l)$ and the two models with the most negative values. This procedure is carried out several times until the final value is computed using four models: two with $\varepsilon - \varepsilon_j < 0$ and two models with $\varepsilon - \varepsilon_j > 0$.

Having derived a value for $\varepsilon(\lambda_s, \lambda_l)$, the next task is to estimate $\varepsilon(\lambda_i, \lambda_l)$. In general, the derived value of $\varepsilon(\lambda_s, \lambda_l)$ will be bracketed by two of the N candidate aerosol models. We then assume that $\varepsilon(\lambda_i, \lambda_l)$ falls between the same two aerosol models proportionately in the same manner as $\varepsilon(\lambda_s, \lambda_l)$. Finally, we also assume that $K[\lambda_i, \rho_{as}(\lambda_i)]$ falls between the two values for these models in the same proportion as $\varepsilon(\lambda_s, \lambda_l)$. These assumptions are required to proceed, and as we shall see, they are not always true. However, to the extent that the actual aerosols are similar in their optical properties to the candidate models, the assumptions appear to be reasonably valid.

In this paper twelve candidate aerosol models are used: the Maritime, Coastal, and Tropospheric models with RH = 50, 70, 90, and 99%. Tables of the $\rho_a(\lambda) + \rho_{ra}(\lambda)$ versus $\rho_{as}(\lambda)$ relationship were constructed by solving the RTE for each model for $\theta_0 = 0$ to 80° in increments of 2.5°, and at 33 values of θ_v. The azimuthal dependence of the reflectance was determined through Fourier analysis. Computations were carried out for eight values of $\tau_a(\lambda_i)$ from 0.05 to 0.8. The total number of separate solutions to the RTE used in the preparation of the tables exceeded 33,000 (including the Urban models described in the next section). To reduce storage, for a given set (θ_0, θ_v) the simulations were fit to

$$\log[\rho_t(\lambda) - \rho_r(\lambda) - t\rho_w(\lambda)] = \log[a(\lambda)] + b(\lambda)\log[\rho_{as}(\lambda)] + c(\lambda)\log^2[\rho_{as}(\lambda)] \tag{13}$$

by least-squares. In the case of the azimuth angle ϕ_v, we expanded $a(\lambda)$, $b(\lambda)$ and $c(\lambda)$ in a Fourier series in ϕ_v and stored only the Fourier coefficients. As the reflectances are even functions of the relative azimuth angle ϕ_v, $a(\lambda)$, $b(\lambda)$, and $c(\lambda)$ will be even functions of ϕ_v. Thus, we can write

$$a(\theta_v, \theta_0, \phi_v, \lambda) = a^{(0)}(\theta_v, \theta_0, \lambda) + 2\sum_{m=1}^{M} a^{(m)}(\theta_v, \theta_0, \lambda)\cos m\phi_v,$$

with

$$a^{(m)}(\theta_v, \theta_0, \lambda) = \frac{1}{\pi}\int_0^{\pi} a(\theta_v, \theta_0, \lambda, \phi_v)\cos m\phi_v \, d\phi_v,$$

etc. Using Fourier analysis with $M = 14$ produced about the same accuracy in the results as interpolating with a division in ϕ_v of 5° or 10°.

2.2.1 Test of the multiple-scattering algorithm

We have tested this multiple-scattering algorithm by applying it to pseudo data created using the *Shettle and Fenn* [1979] Tropospheric, Coastal, Maritime, and Urban models at RH = 80%, denoted by T80, C80, M80, and U80, respectively. Note that these are *not* part of the candidate aerosol set, although the size and refractive index distributions of T80, C80, and M80 are similar to members of the set. In contrast to the others, and unlike any members of the candidate set, U80 has strong aerosol absorption.

Comparison between the single-scattering and multiple-scattering algorithms for pseudo data

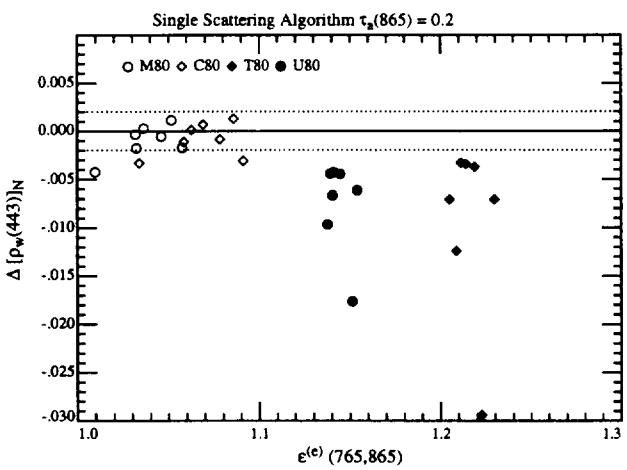

Figure 8a. $\Delta[\rho_w(443)]_N$ as a function of $\varepsilon^{(e)}(765, 865)$ for $\tau_a(865) = 0.2$ and all of the viewing geometries examined in the study, using the single-scattering algorithm.

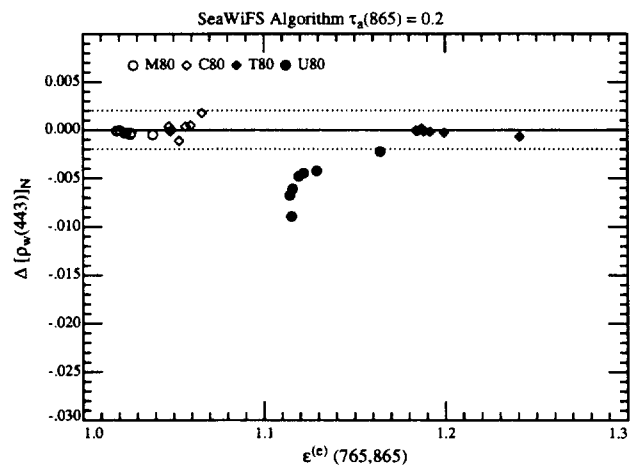

Figure 8b. $\Delta[\rho_w(443)]_N$ as a function of $\varepsilon^{(e)}(765, 865)$ for $\tau_a(865) = 0.2$ and all of the viewing geometries examined in the study, using the multiple-scattering algorithm.

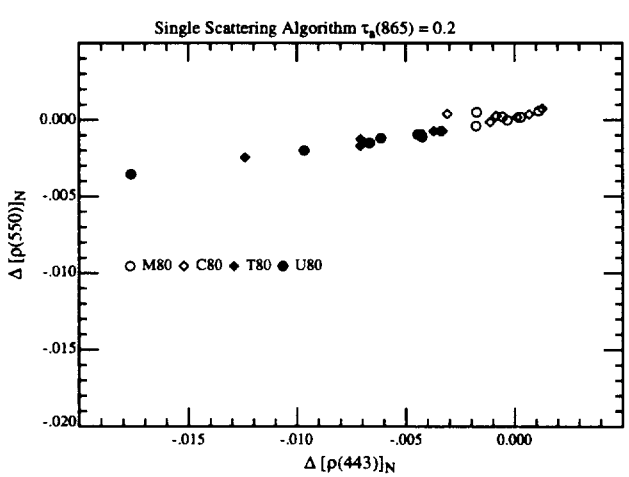

Figure 8c. $\Delta[\rho_w(550)]_N$ as a function of $\Delta[\rho_w(443)]_N$ for the results in Figure 8a.

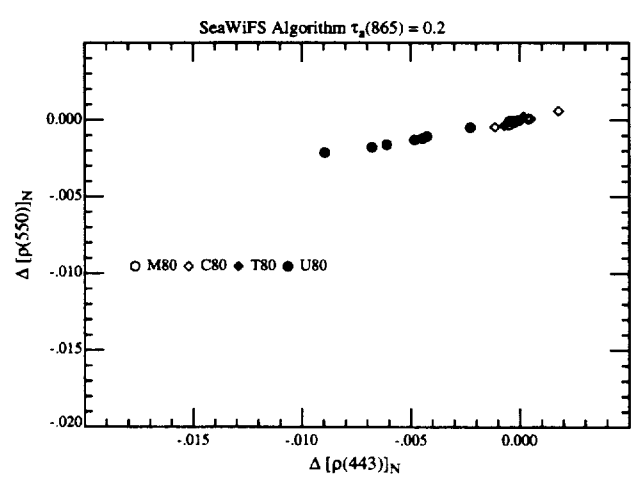

Figure 8d. $\Delta[\rho_w(550)]_N$ as a function of $\Delta[\rho_w(443)]_N$ for the results in Figure 8b.

created with these models at the seven sun-viewing geometries described earlier is provided in Figure 8 for $\tau_a(865) = 0.2$. Clearly, including multiple scattering in the algorithm significantly improves the retrieval of $[\rho_w(443)]_N$ for the T80, C80, and M80 cases, for which $\tau_a(443) \approx 0.50$, 0.32, and 0.24, respectively (Figures 4a and 5). In contrast, the U80 retrievals, although somewhat improved over single scattering, are still very poor. Thus, even though the size distribution of the U80 model is similar to the candidates (both in modal diameter and standard deviation), the fact that the particles are strongly absorbing causes as large an error in the retrieval of $[\rho_w(443)]_N$ as neglecting multiple scattering completely. Clearly, particle absorption must have a profound impact on multiple scattering.

As in Figures 6c and 6d, Figures 8c and 8d provide the relationship between $[\rho_w(550)]_N$ and $[\rho_w(443)]_N$ for the single-scattering and the multiple-scattering (SeaWiFS) algorithms. For the multiple-scattering algorithm, $\Delta[\rho_w(550)]_N \approx (1/4)\Delta[\rho_w(443)]_N$, and with the exception of very low pigment concentrations, the error in atmospheric correction at 443 nm will contribute more significantly to the error in R [Eq. (4)] than that at 550 nm. Fortuitously, the errors at 443 and 550 nm typically have the same sign and, therefore, tend to cancel in R.

Table 2: Mean value of C obtained for seven viewing geometries and three aerosol models (M80, C80, and T80). The number in parenthesis is the standard deviation divided by the mean (in %).

$\tau_a(865)$	$C_{\text{True}} = 0.10$ mg/m^3	$C_{\text{True}} = 0.47$ mg/m^3	$C_{\text{True}} = 0.91$ mg/m^3
0.1	0.101	0.466	0.912
	(1.6)	(3.4)	(9.1)
0.2	0.100	0.470	0.940
	(3.1)	(4.7)	(12.8)
0.3	0.098	0.493	0.936
	(5.5)	(15.3)	(25.3)

The error in the pigment concentration induced by $\Delta[\rho_w(550)]_N$ and $\Delta[\rho_w(443)]_N$ in the multiple-scattering algorithm is provided in Table 2. To prepare this table, the errors were added to values of $[\rho_w(550)]_N$ and $[\rho_w(443)]_N$ that are characteristic of three pigment concentrations

(0.10, 0.47, and 0.91 mg/m^3) in order to produce retrieved reflectances that include the atmospheric correction error. These were then inserted into Eq. (4) and the resulting pigment concentration was derived for each sun-viewing geometry for the M80, C80, and T80 aerosol models. For each true pigment concentration, the twenty-one retrieved values of C (seven geometries times three aerosol models) were averaged and the standard deviation was computed. The computations were carried out for $\tau_a(865) = 0.1$, 0.2, and 0.3.

As expected, the quality of the retrievals is best for the smallest value of $\tau_a(865)$. Excellent retrievals of C (as indicated by excellent mean values and small relative standard deviations) were obtained for $\tau_a(865) = 0.1$ and 0.2, and for the two lower concentrations for $\tau_a(865) = 0.3$. As mentioned earlier, $\tau_a(865)$ is typically $\lesssim 0.2$ in regions not subjected to urban pollution or desert dust. For $\tau_a(865) = 0.3$ and a true value of C of 0.91 mg/m^3, one retrieved value of C was ≈ 9 mg/m^3 ($\theta_0 = 60°$, $\theta_v \approx 45°$, T80, for which $\tau_a(443) \approx 0.75$ and $\tau_a(550) \approx 0.6$). This value was not included in the average or the standard deviation computation. These results suggest that the multiple-scattering algorithm will provide excellent results as long as the candidate aerosol models are similar in size and composition to the aerosol actually present.

2.2.2 Effect of absorption on multiple scattering

To try to understand the effect of particle absorption on multiple scattering, a set of multiple scattering computations of $\rho_a + \rho_{ra}$ was carried out in which particle absorption *alone* was varied. Specifically, we used the phase functions for the T50 and M99 aerosol models evaluated at 865 nm (Figure 9). These models have the most weakly (T50) and the most strongly (M99) forward peaked scattering phase function among the candidate models. Simulations of $\rho_a + \rho_{ra}$ as a function of τ_a (or equivalently ρ_{as}) were made for $\theta_0 = 60°$ and $\theta_v \approx 1°$, with $\tau_r = 0.015$ (865 nm) and 0.236 (443 nm), as ω_a assumed the values of 0.6, 0.8, and 1.0. The results are presented in Figure 10. Two facts concerning the $\rho_a + \rho_{ra}$ versus ρ_{as} relationship emerge from these simulations. First, for $\omega_a = 1$, the relationship is nearly linear and, for the sharply peaked M99 phase

function, the Rayleigh-aerosol interaction ($\sim$ the difference between the dashed and solid curves

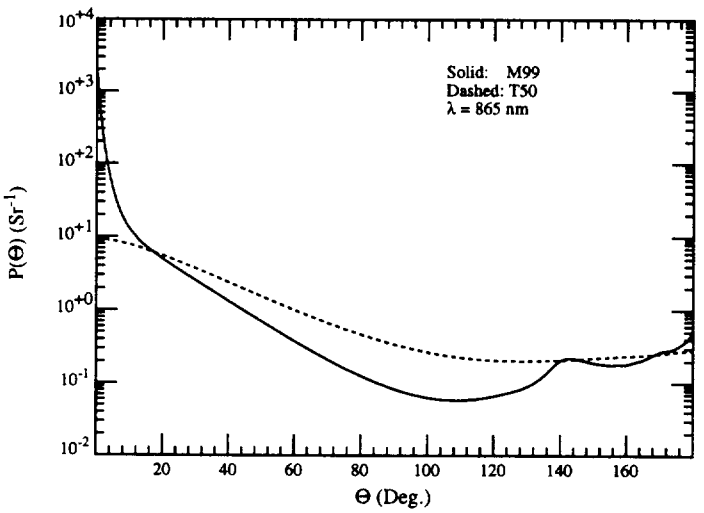

Figure 9. Scattering phase functions for the T50 and M99 aerosol models at 865 nm.

caused by changing τ_r) is small, while for the smoother T50 phase function the Rayleigh-aerosol interaction is significantly larger. This is to be expected, since the mid-angle scattering by T50 is much larger than M99 (Figure 9). Second, as ω_a decreases, there are greater departures from linearity and an increase in the significance of the Rayleigh-aerosol interaction for *both* T50 and

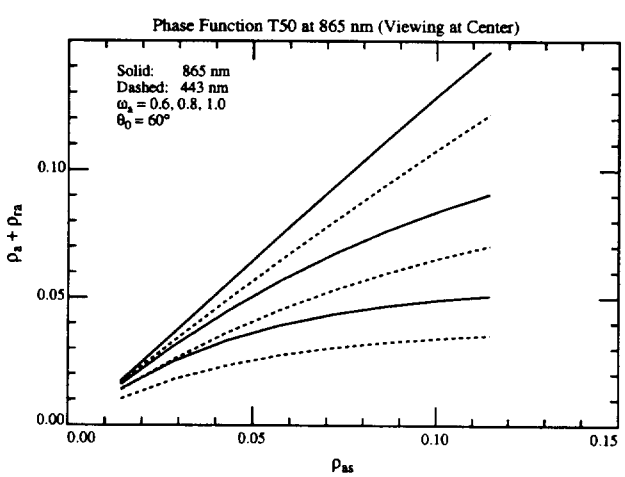

Figure 10a. $\rho_a + \rho_{ra}$ as a function of ρ_{as} and ω_a for 443 nm (dashed) and 865 nm (solid) and the T50 phase function. Curves from bottom to top correspond to ω_a = 0.6, 0.8, and 1.0.

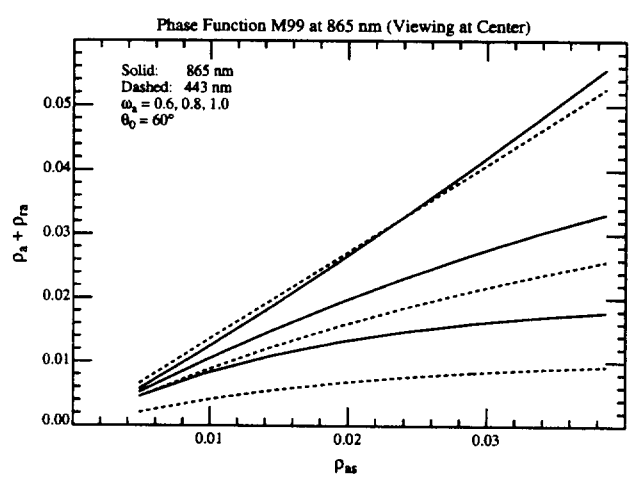

Figure 10b. $\rho_a + \rho_{ra}$ as a function of ρ_{as} and ω_a for 443 nm (dashed) and 865 nm (solid) and the M99 phase function. Curves from bottom to top correspond to ω_a = 0.6, 0.8, and 1.0.

M99. The general shape of the curves is explained by the fact that $\rho_a + \rho_{ra}$ must approach an

asymptotic value as $\tau_a \rightarrow \infty$. Also, increasing τ_r causes more diffuse light to enter the aerosol layer and traverse longer paths through it, with the concomitant greater chance of absorption. This explains the strong influence of ω_a on ρ_{ra}.

The impact of the absorption in Figure 10 is serious. Consider a hypothetical situation in which the M99 phase function is appropriate and $\epsilon(\lambda_i, \lambda_l) = 1$, so $\rho_{as}(\lambda_i) = \rho_{as}(\lambda_l)$. Also, assume that $\epsilon(\lambda_i, \lambda_l)$ is correctly determined by the algorithm and that $\rho_a + \rho_{ra} \approx 0.02$ at 865 nm. Then, if $\omega_a = 1$ were used for estimating $\rho_a + \rho_{ra}$ at 443 nm, but the true value of ω_a was actually 0.8, Figure 10b shows that the error in $\rho_a + \rho_{ra}$ at 443 nm would be ~ -0.004. In contrast, if the $\omega_a = 1$ assumption was correct the error would be $\sim +0.001$. Clearly, the effect of absorption is to produce large negative errors in $t\rho_w$, i.e., to over estimate the effect of the atmosphere. Figure 3a suggests that when $\epsilon(\lambda_i, \lambda_l)$ is estimated from $\epsilon(\lambda_s, \lambda_l)$ using weakly- or nonabsorbing aerosol models, it will be overestimated, i.e., $\epsilon(\lambda_i, \lambda_l)$ will be too large, if the aerosol strongly absorbs. This effect will cause a further over estimation of the atmospheric effect.

As the twelve candidate models in Subsection 2.2.1 are combinations of two components with physical properties dependent on RH, they represent a fixed set of values of ω_a at each wavelength, i.e., there are only twelve different values of ω_a. At 865 nm, these range from 0.99857 (M99) to 0.92951 (T50). Furthermore, each model possesses a unique value of $\varepsilon(\lambda_s, \lambda_l)$ and a more or less unique value of $\varepsilon(\lambda_i, \lambda_l)$ for a given sun-viewing geometry (Figure 3a). Thus, the choice of the twelve candidates forces a definite relationship between ω_a and $\varepsilon(\lambda_i, \lambda_l)$. In the case of the twelve models chosen here, there is a steady decrease in ω_a with increasing $\varepsilon(\lambda_i, \lambda_l)$. If this relationship is more or less correct, an excellent correction is effected (Figure 8b, T80); however, with its low value of ω_a (0.74806 for U80 at 865 nm) the Urban model falls considerably outside this relationship and the resulting atmospheric correction is very poor (U80 in Figure 8b). This is further shown in Figure 11 in which the multiple-scattering algorithm is applied to the Haze C models. In this Figure we have limited the models to those that fall within the range of variation of the values of $\varepsilon(\lambda_s, \lambda_l)$ of the candidate models, and also models for which $\tau_a(443) \lesssim 0.8$, the upper limit of τ_a used in the preparation of the $\rho_a + \rho_{ra}$ versus ρ_{as} look up tables. Haze C models with a real index of refraction ($\omega_a = 1$) and $\nu \geq 3$ do not follow the $\omega_a - \varepsilon(\lambda_s, \lambda_l)$ relationship implied by the candidate models, and the values of $\Delta[\rho_w(443)]_N$ are positive. In contrast, the dust and mineral models both display ω_a-values less than T50, and for these the $\Delta[\rho_w(443)]_N$ are large and negative. Thus, it should be clear that it is imperative to use candidate aerosol models

that possess an approximately correct relationship between ω_a and $\varepsilon(\lambda_s, \lambda_l)$, or physically, an approximately correct relationship between particle size and absorption. Such a relationship must be based on climatology, e.g., when the aerosol optical thickness over the North Atlantic Saharan

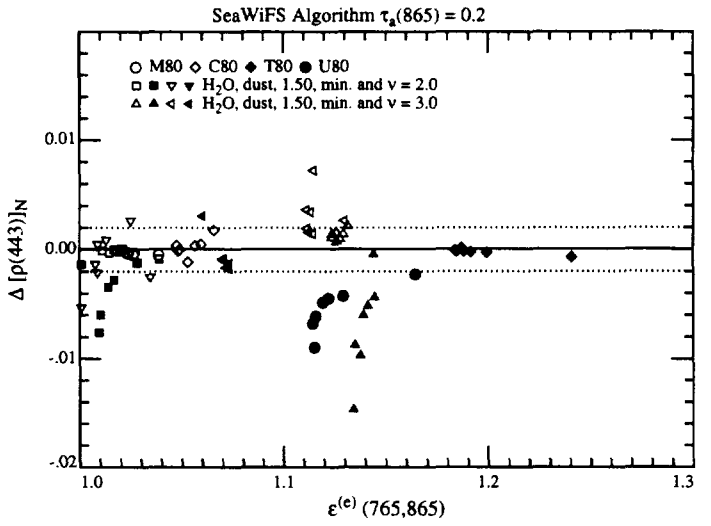

Figure 11. $\Delta[\rho_w(443)]_N$ as a function of $\varepsilon^{(e)}(765, 865)$ for the Haze C models with $\tau_a(865) = 0.2$ and all of the viewing geometries examined in the study, using the multiple-scattering algorithm.

dust zone is high, one should use candidate models consisting of a linear combination of a Maritime model and Saharan dust model, either uniformly mixed in the marine boundary layer or having a two-layer structure. Given such climatology-based models, preparation of the appropriate lookup tables for incorporation into the algorithm is a simple process.

As an example, we modified the algorithm to utilize only four candidate models, the *Shettle and Fenn* [1979] Urban models at RH = 50%, 70%, 90%, and 99%, and tested it using pseudo data created with the U80 model. In this manner, the ω_a and $\varepsilon(\lambda_s, \lambda_l)$ relationship was approximately correct. The results are provided in Figure 12, which shows the error in $[\rho_w(443)]_N$ as a function of the aerosol optical thickness of U80 at 865 nm. Recall, from Figure 4a, that $\tau_a(443) \approx 1.75\tau_a(865)$. Comparison with Figure 11, for which $\tau_a(865) = 0.2$, shows that the maximum error (which occurs at the scan edge with $\theta_0 = 60°$), when the Urban models are used as candidates, is only twice the minimum error when the original twelve candidate aerosol models were used. This

underscores the necessity of having realistic climatologically-based aerosol models in situations in

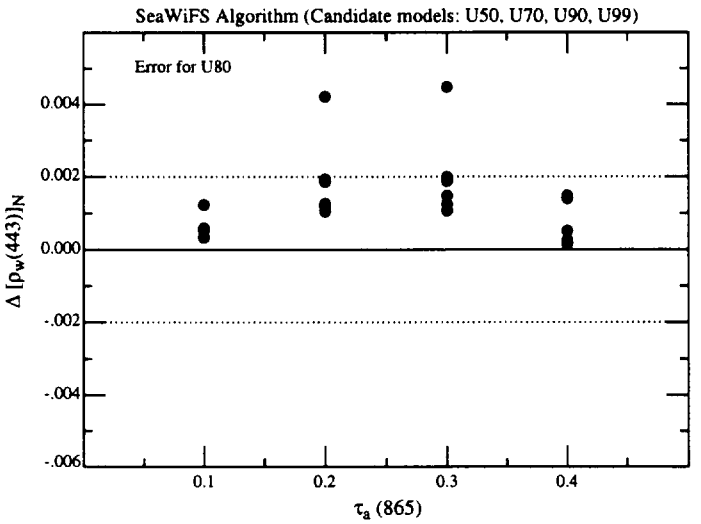

Figure 12. $\Delta[\rho_w(443)]_N$ as a function of $\tau_a(865)$ for the U80 model, when the candidate aerosol models in the multiple-scattering algorithm are restricted to U50, U70, U90, and U99.

which the aerosol concentration is sufficiently large to require consideration of multiple scattering. We shall discuss experimental efforts to obtain such a climatology in a later section.

3. Examination of the approximations

In this Section we assume that the appropriate set of candidate aerosol models can be selected in a given situation and examine the effects of the approximations made in Section 2. These include the influence of whitecaps on the sea surface, the influence of the vertical distribution of the aerosol, the approximation of the atmosphere as a plane-parallel medium, i.e., ignoring the curvature of the earth, the use of scalar radiative transfer theory (ignoring polarization) in preparation of the multiple-scattering lookup tables, and the effect of ignoring sea-surface roughness in the preparation of the lookup tables.

3.1 Whitecaps

As mentioned earlier, the term $t(\lambda_i)\rho_{wc}(\lambda_i)$ in Eq. (6) has been ignored in the development of the algorithm. If we indicate the reflectance measured at the top of the atmosphere as $\rho_t^{(m)}$,

this reflectance consists of two parts; that which would be measured in the absence of whitecaps, and the reflectance added by the whitecaps $t\rho_{wc}$, i.e.,

$$\rho_t^{(m)} = \rho_t + t\rho_{wc}. \tag{14}$$

Since the retrieval algorithms developed in Section 2 must be operated with ρ_t rather than $\rho_t^{(m)}$, $t\rho_{wc}$ must be removed from the imagery *before* the algorithm can be applied.

As in the case of the normalized water-leaving radiance, we define the normalized whitecap reflectance (or the albedo) $[\rho_{wc}]_N$ to be the area-weighted reflectance (over several pixels) of oceanic whitecaps *at* the sea surface in the absence of the atmosphere. Then the whitecap component of the radiance leaving the surface is

$$L_{wc}(\lambda) = [\rho_{wc}(\lambda)]_N \frac{F_0 \cos\theta_0}{\pi} t(\theta_0, \lambda),$$

where the whitecaps are assumed to be lambertian. Converting to reflectance we have

$$\rho_{wc}(\lambda) = [\rho_{wc}(\lambda)]_N \, t(\theta_0, \lambda).$$

At the top of the atmosphere, the whitecaps contribute

$$t\rho_{wc}(\lambda) = [\rho_{wc}(\lambda)]_N \, t(\theta_0, \lambda) t(\theta_v, \lambda).$$

The problem faced in removing $t\rho_{wc}(\lambda)$ from $\rho_t(\lambda)$ in Eq. (6) is the estimation of $[\rho_{wc}(\lambda)]_N$.

Based on previous research on the relationship between whitecaps and environmental parameters, the algorithm adopted for estimating $[\rho_{wc}]_N$ is that of *Koepke* [1984] [*Gordon and Wang*, 1994b]:

$$[\rho_{wc}]_N = 6.49 \times 10^{-7} \, W^{3.52}, \tag{15}$$

where W is the wind speed in m/s measured 10 m above the sea surface. *Gordon and Wang* [1994b] show that, for a given wavelength, this predicts $[\rho_{wc}]_N$ with a standard deviation approximately equal to $[\rho_{wc}]_N$ itself.

The effect of the any error in the estimation of $[\rho_{wc}]_N$ on the retrieved water-leaving reflectance is strongly dependent on the spectral variation of $[\rho_{wc}(\lambda)]_N$. In *Gordon and Wang* [1994b] it was assumed, based on measurements carried out by *Whitlock, Bartlett and Gurganus* [1982], that $[\rho_{wc}(\lambda)]_N$ was independent of λ; however, *Schwindling* [1995] and *Frouin, Schwindling and*

Deschamps [1995] have reported measurements on breaking waves in the surf zone suggesting that whitecaps may reflect considerably less in the NIR than in the visible, presumably because a significant component of the whitecap reflectivity is due to scattering from submerged bubbles. To understand the effect of spectral variation in $[\rho_{wc}]_N$ on the accuracy of atmospheric correction, the multiple scattering algorithm has been operated in the presence of whitecaps displaying both nonspectral reflectance and the spectral reflectance suggested by *Frouin, Schwindling and Deschamps* [1995]. Figure 13 compares the error in $[\rho_w(443)]_N$ as a function of θ_0 for viewing at the edge of the MODIS scan with the M80 aerosol model ($\tau_a(865) = 0.2$) for these two cases when the error in the *estimate* of $[\rho_{wc}]_N$ at 443 nm is ± 0.002. This error in $[\rho_{wc}(443)]_N$ corresponds to a wind speed of $\sim 8 - 9$ m/s. Figure 13 shows that for wavelength-independent whitecap reflectivity, the resulting error in $[\rho_w(\lambda)]_N$ can be significantly less than ($\sim 1/4$) the error in the estimate of $[\rho_{wc}(443)]_N$. In contrast, if whitecaps reflect in a manner consistent with the

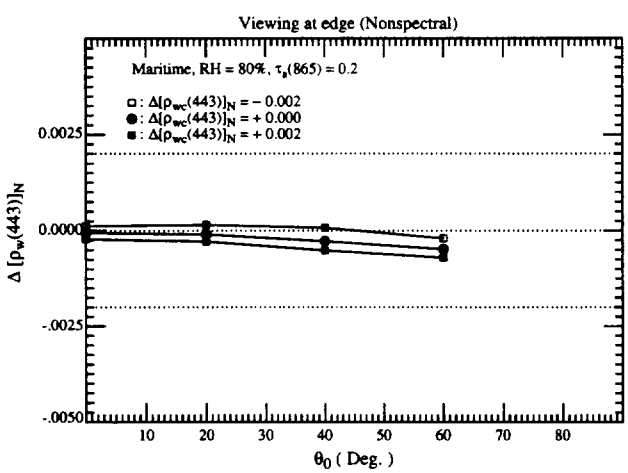

Figure 13a. $\Delta[\rho_w(443)]_N$ as a function of the error in the whitecap reflectance at 443 nm and θ_0 at the edge of the scan for the M80 aerosol model with $\tau_a(865) = 0.2$. Whitecap reflectance spectrum is that proposed by *Whitlock, Bartlett and Gurganus* [1982].

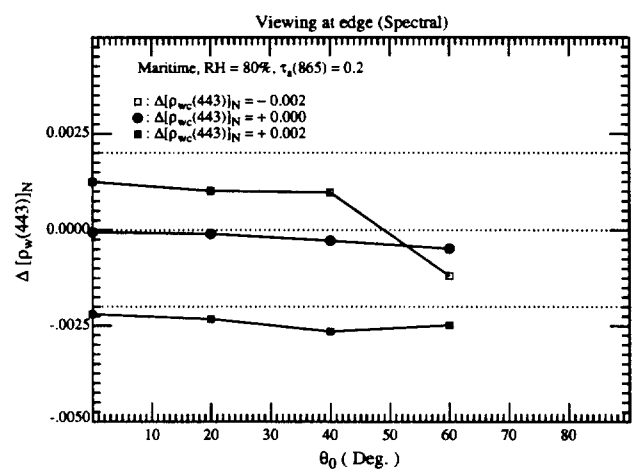

Figure 13b. $\Delta[\rho_w(443)]_N$ as a function of the error in the whitecap reflectance at 443 nm and θ_0 at the edge of the scan for the M80 aerosol model with $\tau_a(865) = 0.2$. Whitecap reflectance spectrum is that proposed by *Frouin, Schwindling and Deschamps* [1995].

Frouin, Schwindling and Deschamps [1995] observations, the error in $[\rho_w(443)]_N$ can be expected to be of the same order-of-magnitude as the error in $[\rho_{wc}(443)]_N$. Similar simulations using the T80 aerosol model, for which $\varepsilon(\lambda, 865)$ displays strong variation with λ, show similar effects for the case of whitecaps with the *Frouin, Schwindling and Deschamps* [1995] reflectance; however, the error for the *Whitlock, Bartlett and Gurganus* [1982] reflectance model can also be the same order of magnitude as $\Delta[\rho_{wc}(443)]_N$ [*Gordon and Wang*, 1994b]. Figure 13 shows that an overestimation of $[\rho_{wc}(443)]_N$ leads to a negative error in $[\rho_w(443)]_N$. The same is true at 550 nm.

When the errors in $[\rho_w(\lambda)]_N$ are negative, algorithms such as Eq. (4), that use radiance ratios, can lead to very large errors in the derived products. Because of this, it is better to underestimate the $[\rho_{wc}(443)]_N$ in the whitecap correction algorithm rather than overestimating it.

As whitecaps have the potential of producing errors of a magnitude similar to the magnitude of the acceptable error in $[\rho_w(\lambda)]_N$, it is important to obtain radiometric data of actual oceanic whitecaps, and validate its dependence on wind speed.

3.2 Aerosol vertical structure

The reflectance of the atmosphere in the single-scattering approximation is independent of the manner in which the aerosol is distributed with altitude. However, this independence does

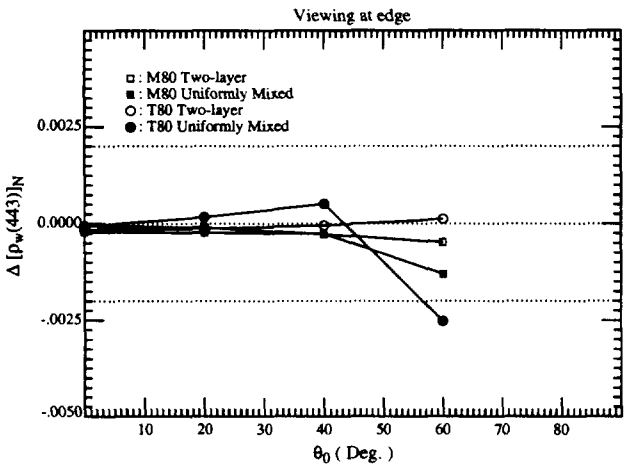

Figure 14a. Effect of the vertical distribution of aerosol on $\Delta[\rho_w(443)]_N$ as a function of θ_0 at the edge of the scan for the T80 and M80 aerosol models with $\tau_a(865) = 0.2$. Note that the correction algorithm assumes that the "Two-layer" stratification is correct.

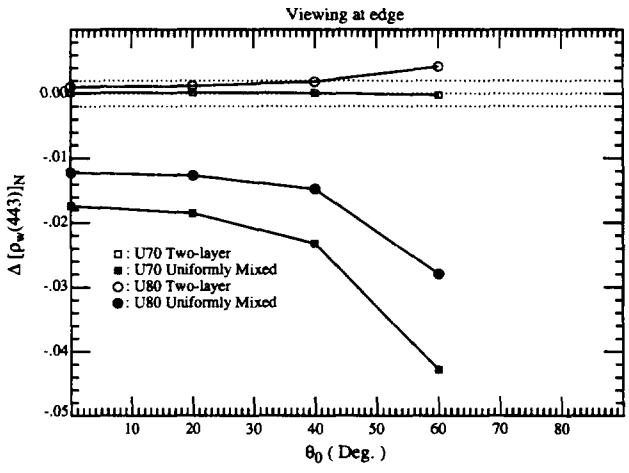

Figure 14b. Effect of the vertical distribution of aerosol on $\Delta[\rho_w(443)]_N$ as a function of θ_0 at the edge of the scan for the U80 and U70 aerosol models with $\tau_a(865) = 0.2$. Note that the correction algorithm assumes that the "Two-layer" stratification is correct.

not extend to a multiple-scattering atmosphere. As the multiple-scattering algorithm assumes that the aerosol is all located in the bottom layer of a two-layer atmosphere, it is important to understand the effect of aerosol vertical structure on the correction algorithm. This has been studied by comparing the error in the algorithm when the pseudo data are simulated using the "correct" two-layer model with the error when the pseudo data are simulated using a model in which the aerosol and Rayleigh scattering have an altitude-independent mixing ratio, i.e., a uniformly mixed model. Figure 14a provides such a comparison for the M80 and T80 aerosol models

with $\tau_a(865) = 0.2$. It is seen that the effect of an incorrect assumption regarding the vertical structure will not lead to serious errors in this case. However, in the case of strongly absorbing aerosols, e.g., the Urban models, the assumed vertical structure is very important. Figure 14b provides the two-layer versus uniformly mixed cases for the Urban models with $\tau_a(865) = 0.2$. In this case the candidate aerosol models were restricted to U50, U70, U90, and U99, as in the results for Figure 12. For the U80 case, the error becomes excessive, increasing by over an order of magnitude compared to the two-layer case. More disturbing is the performance of the U70 aerosol model. U70 is actually one of the candidate aerosol models in this case. When the vertical structure is the same as assumed by the algorithm, the error is negligible. In contrast, when the incorrect structure is assumed, the error becomes very large.

As we have examined only an extreme deviation from that assumed by the correction algorithm, it is of interest to quantify how the correction algorithm performs as the aerosol layer thickens from being confined just near the surface to being mixed higher in the atmosphere. Thus, the top-of-atmosphere reflectance was simulated using a two layer model with aerosol *plus* Rayleigh scattering in the lower layer and *only* Rayleigh scattering in the upper layer. The fraction of the Rayleigh scattering optical thickness assigned to the lower layer was consistent with aerosol-layer thickness of 0, 1 km, 2 km, 4 km, 6 km, and ∞. The aerosol model used in the simulations was U80, and $\tau_a(865)$ was kept constant at 0.2. The multiple-scattering algorithm was then operated with this pseudo data using U50, U70, U90, and U99 as candidate models. The results of this exercise are provided in Figure 15. Clearly, progressive thickening of the layer in which the aerosol resides leads to a progressive increase in the error in the retrieved water-leaving reflectance.

This influence of vertical structure on the algorithm when the aerosol is strongly absorbing is easy to understand. The algorithm assumes all of the aerosol resides in a thin layer beneath the molecular scattering layer. As the aerosol layer thickens and encompasses more and more of the molecular scattering layer, the amount of Rayleigh scattering within the aerosol layer will increase causing an increase in the average path length of photons through the layer, and a concomitant increase in absorption. Thus, for a given τ_a, ρ_t will decrease as the thickness of the aerosol layer increases. Since $\rho_r \sim \lambda^{-4}$, this decrease will be relatively more in the visible than in the NIR, so the algorithm will predict values of $\rho_a + \rho_{ra}$ in the visible that are too large, yielding an over correction, $\Delta[\rho_w(443)]_N < 0$.

Ding and Gordon [1995] (Figures 9 and 10) have provided some examples of the error in the multiple-scattering algorithm for vertical structures in which the aerosol model as well as concentration varies with altitude. For the weakly-absorbing aerosol of the models that they inves-

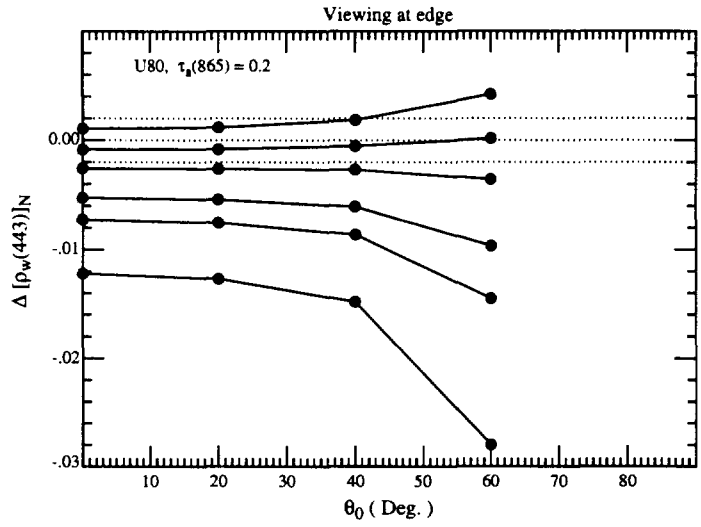

Figure 15. Effect of the vertical distribution of aerosol on $\Delta[\rho_w(443)]_N$ as a function of θ_0 at the edge of the scan for the U80 aerosol models with $\tau_a(865) = 0.2$. Curves from top to bottom refer to situations in which the aerosol is confined to a layer just above the surface, between the surface and 1, 2, 4, and 6 km, and uniformly mixed throughout the atmosphere.

tigated ($\omega_a \gtrsim 0.93$), the conclusions are similar to those here: as long as the aerosol is weakly absorbing, the error is negligible, but as ω_a decreases, the error becomes progressively larger. Clearly, more study is required for a quantitative assessment of the impact of vertical structure in a strongly absorbing atmosphere; however, the computations provided here demonstrate that a large error in the vertical structure of the aerosol layer assumed for the lookup tables will result in a very poor atmospheric correction, even if the candidate aerosol models are appropriate. Figure 15 suggests that at a minimum, the lookup tables for the Urban candidates need to be recalculated under the assumption of an aerosol layer of finite physical thickness, i.e., some Rayleigh scattering in the aerosol layer. It also suggests that, for the case studied, if the lookup tables were computed for an aerosol layer of physical thickness 2 km, they would provide reasonable retrievals for layers with thicknessess from 1 to 3 km, i.e., the algorithm could tolerate a ± 1 km error in the layer thickness for this case.

3.3 Earth curvature

All atmospheric corrections algorithms developed thus far ignore the curvature of the earth, i.e., the plane-parallel atmosphere approximation has been used in the radiative transfer simulations. However, at the level of accuracy required to utilize the full sensitivity of MODIS, it may be necessary to take the curvature of the earth into account, especially at high latitudes with their associated large θ_0 values. *Ding and Gordon* [1994] have examined this problem in detail using a model based on a spherical shell atmosphere solved with Monte Carlo techniques. It was found that as long as ρ_r was computed using a spherical shell atmosphere model, the multiple-scattering algorithm performed as well at high latitudes as at low latitudes. They provided a method for the rapid computation of ρ_r for the spherical shell atmosphere; however, it has yet to be implemented for image processing.

3.4 Polarization

All of the radiative transfer simulations described in Section 2 were carried out using scalar radiative transfer theory, i.e., polarization was ignored. In the case of single scattering, except for the terms involving the Fresnel reflectance, scalar (ignores polarization) and vector (includes polarization) radiative transfer theory lead to the same radiances. Thus, the single scattering algorithm is little influenced by polarization. It is well known, however, that, when multiple scattering is present, the use of scalar theory leads to small errors ($\sim$ few %) in the radiance compared to that computed using exact vector theory [*Gordon, Brown and Evans*, 1988; *Kattawar, Plass and Hitzfelder*, 1976]. As with CZCS, in the actual application of the algorithm, ρ_r will be computed using vector theory; however, the lookup tables relating $\rho_a + \rho_{ra}$ to ρ_{as} have been computed using scalar theory. To understand the influence of neglecting polarization in the computation of the lookup tables, simulations of the top-of-the-atmosphere reflectance ρ_t were carried out using both scalar and vector radiative transfer theory. In the case of the scalar simulations, $[\rho_w(443)]_N$ was retrieved as described in Section 2.1.2. An identical retrieval procedure was used for the vector simulations with a single exception: as in the case of CZCS, ρ_r was computed using vector theory. The results are presented in Figure 16a and 16b for the M80 and T80 aerosol models respectively. These figures provide $\Delta\rho \equiv t\Delta\rho_w(443)$ (rather than $\Delta[\rho_w(443)]_N$ in the previous figures) produced by the multiple-scattering correction algorithm as a function

of θ_0 for $\tau_a(865) = 0.2$. The notation "S–S" and "V–V" means that *both* ρ_t and ρ_r were computed using scalar (S–S) and vector (V–V) radiative transfer theory, respectively. Note that the difference between computations is the error induced by ignoring polarization in the preparation of the $\rho_a + \rho_{ra}$ versus ρ_{as} lookup tables. At present, only a small number of simulations of the type shown in Figure 16 have been carried out; however, for these the difference between S–S and V–V was typically $\lesssim 0.001$ but reached as much as 0.002 in isolated cases. Thus, compared to

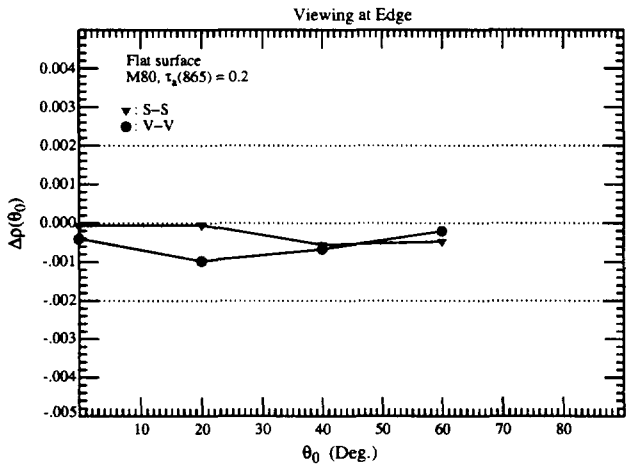

Figure 16a. Effect of neglecting polarization in the multiple-scattering lookup tables. S–S and V–V are for ρ_t and ρ_r computed using scalar and vector radiative transfer theory, respectively. $\Delta\rho \equiv t\Delta\rho_w$, the aerosol model is M80, and $\tau_a(865) = 0.2$.

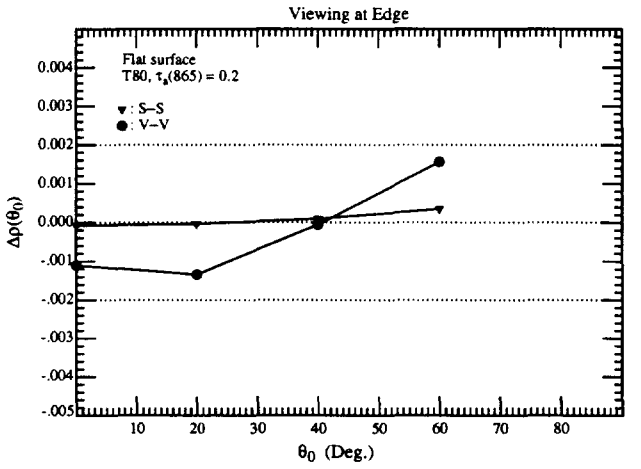

Figure 16b. Effect of neglecting polarization in the multiple-scattering lookup tables. S–S and V–V are for ρ_t and ρ_r computed using scalar and vector radiative transfer theory, respectively. $\Delta\rho \equiv t\Delta\rho_w$, the aerosol model is T80, and $\tau_a(865) = 0.2$.

the errors possible when strongly absorbing aerosols or whitecaps are present, this error appears negligible. It could be removed by recomputing the lookup tables using vector radiative transfer theory, but at considerable computational cost.

3.5 Sea surface roughness

The roughness of the sea surface caused by the wind can play a large role on the reflectance measured at the top of the atmosphere. The principal effect of the rough surface is to redirect the direct solar beam reflected from the sea surface into a range of angles. This leads to a very large reflectance close to the specular image of the sun, know as sun glitter or the sun's glitter pattern. As this can be many times the radiance exiting the atmosphere in the smooth-surface case, the data in the region of the sun glitter must be discarded. This is accomplished by a mask as described in Appendix A. The remainder of the rough-surface effect is due to a redistribution

of light scattered from the reflected solar beam (because it is redirected) and a redistribution of sky light reflected from the surface (the Fresnel reflection terms in Eq. (9)). This redistribution of radiance contaminates the imagery over all viewing angles. As the lookup tables relating

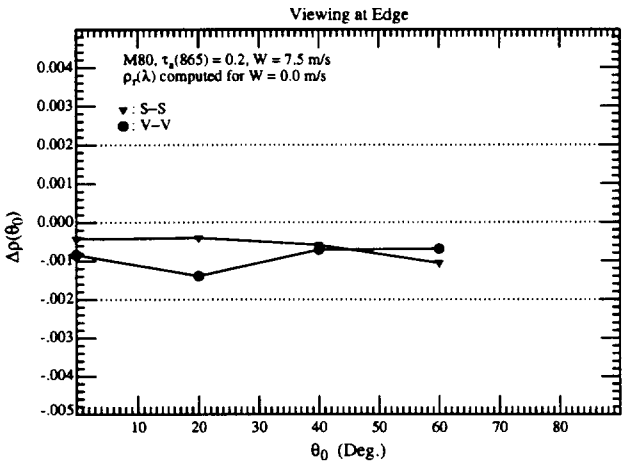

Figure 17a. Effect of neglecting sea surface roughness in the multiple-scattering lookup tables. S–S and V–V are for ρ_t and ρ_r computed using scalar and vector radiative transfer theory, respectively. $\Delta\rho \equiv t\Delta\rho_w$, the aerosol model is M80, and $\tau_a(865) = 0.2$. ρ_r has been computed assuming that $W = 0.0$ m/s.

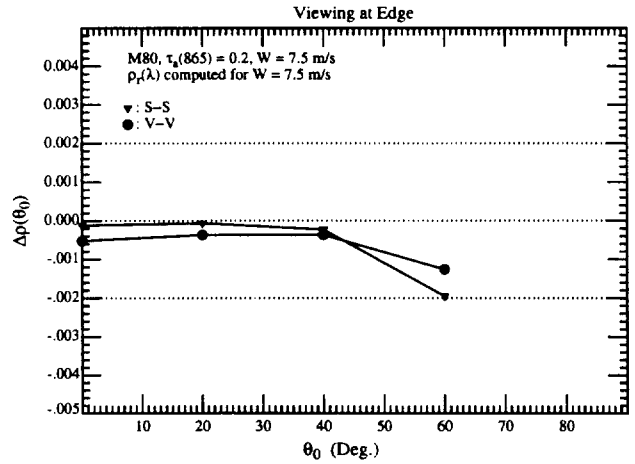

Figure 17b. Effect of neglecting sea surface roughness in the multiple-scattering lookup tables. S–S and V–V are for ρ_t and ρ_r computed using scalar and vector radiative transfer theory, respectively. $\Delta\rho \equiv t\Delta\rho_w$, the aerosol model is M80, and $\tau_a(865) = 0.2$. ρ_r has been computed assuming that $W = 7.5$ m/s.

$\rho_a + \rho_{ra}$ to ρ_{as} were computed under the assumption that the surface was flat, it is necessary to examine the error in the water-leaving reflectance induced when viewing a rough ocean. This was effected by computing ρ_t for an ocean roughened by the wind and inserting the result into the multiple-scattering correction algorithm. In this simulation, the sea surface roughness was based on the *Cox and Munk* [1954] surface slope distribution function (Appendix A). For computational simplicity, an omnidirectional wind was assumed [*Cox and Munk*, 1954]. The wind speed was taken to be $\sim$ 7.5 m/s. Since *Gordon and Wang* [1992b] and *Gordon and Wang* [1992a] showed that at the radiometric sensitivity of SeaWIFS and MODIS, correct computation of the influence of surface roughness on ρ_r required use of vector radiative transfer theory, the computations were carried out using *both* scalar and vector theory. Sample results from one set of the small number of simulations that have been carried out to assess the effect of surface roughness are provided in Figure 17. These are in the same format as Figure 16. The differences between the two panels is that, in Figure 17a ρ_r has been computed assuming a smooth sea surface (a wind speed of zero), while in Figure 17b it has been computed using the correct (7.5 m/s) wind speed. For reference, Figure 16a provides similar results for a smooth sea surface. Comparing Figures 16a

and 17a shows that the residual effect of the rough surface external to the sun's glitter pattern is small ($\Delta\rho \sim 0.0005$), and comparing Figures 16a and 17b shows that the residual effect can be removed by using the correct wind speed in the computation of ρ_r, i.e., ignoring the surface roughness in computation of the lookup tables relating $\rho_a + \rho_{ra}$ to ρ_{as} does not appear to lead to significant error.

4. Remaining issues

We now examine remaining issues in developing and operating the multiple-scattering algorithm. These include the appropriateness of the candidate aerosol models, absorbing aerosols, the effects of stratospheric aerosols, the influence of any sensitivity the sensor might have to the polarization of the top-of-atmosphere reflectance, the angular distribution of the water-leaving reflectance and its influence on the diffuse transmittance, and the effect of sensor calibration errors.

4.1 Appropriateness of aerosol models

Operation of the multiple-scattering algorithm requires a set of candidate aerosol models. Thus far, models from, or derived from, the work of *Shettle and Fenn* [1979] have been used as candidates. These models were basically developed from the analysis of aerosol physical-chemical properties and are believed to provide realistic approximations to the extinction and absorption cross section of real aerosols. However, they have never been validated for the role they are being used for here, i.e., for their ability to provide realistic aerosol phase functions and their spectral variation. As it is important to utilize as candidates, aerosol models that closely approximate the optical properties of actual aerosols over the ocean, work is being carried out or planned to study the optical properties of aerosols over the ocean.

Measurements over and above aerosol optical thickness and its spectral variation are required to understand the adequacy of candidate aerosol models. *Schwindling* [1995] compared estimates of the aerosol scattering phase function obtained from a pier at Scripps Institution of Oceanography at La Jolla, CA, with the properties of the *Shettle and Fenn* [1979] models and concluded that within the accuracy of their measurements the models fit both the phase function and the spectral variation of the aerosol optical thickness. It was also confirmed that $\tau_a(\lambda)$

becomes very low off the coast of CA. Such measurements need to be carried out in different regions and at different times. The aerosol monitoring network based on CIMEL sun/sky radiometers operated by B. Holben [*Holben et al.*, 1996] of NASA/GSFC is presently being expanded to include stations at the coast and on small islands. The plan is to use the methods developed by *Wang and Gordon* [1993] to invert the sky radiance and optical thickness data to obtain the aerosol scattering phase function and the single scattering albedo.

4.2 Absorbing aerosols

In Subsection 2.2.2 it was shown that in the presence of strongly absorbing aerosols, the candidate aerosol models must be restricted to those with values of ω_a similar to the true aerosol. This was effected there by limiting the candidate models to U50, U70, U90, and U99 when the test aerosol was U80 (Figure 12), since when the initial twelve candidate models were used, the error was excessive (Figure 11). Without a method of determining the absorption characteristics of the aerosols from satellite measurements, an aerosol climatology is required to be able to provide realistic candidate models. Furthermore, in Subsection 3.2 it was shown that, for strongly absorbing aerosols, even given the appropriate set of candidate models, knowledge of the vertical distribution of the aerosol was required for an adequate correction (Figure 15). Thus the aerosol climatology needs to contain information concerning the aerosol-layer thickness for regions with strongly absorbing aerosols.

The effort toward building a climatology for absorbing aerosols involves measurements of the type discussed in Subsection 4.1, i.e., measurements of sky radiance and aerosol optical thickness from ships or small islands in the appropriate regions. The *Wang and Gordon* [1993] retrieval algorithm should perform as well for strongly-absorbing as for nonabsorbing aerosols. A climatology for the aerosol vertical distribution can most effectively be built using LIDAR measurements [*Sasano and Browell*, 1989]. An excellent start toward a vertical distribution climatology can be made utilizing data from the Lidar In-Space Technology Experiment (LITE) [*McCormick*, 1995]. On the basis of LITE-based and aircraft-based measurements *Grant et al.* [1995] observed that the Saharan dust layer over the Eastern Caribbean extended in altitude from 1-4 km. This is in contrast to the dust-free atmosphere in which the thickness of the marine boundary layer is typically 1-2 km. Examining a LITE pass from Wallops Island, Virginia to Bermuda, *Ismail et al.* [1995] found that the plume of pollution from the U.S. East Coast was in a 1-2 km thick layer

above the 0.5-1.0 km thick maritime boundary layer. These observations suggest that the principal absorbing aerosols expected in the Atlantic are mixed higher in the atmosphere than assumed in the existing candidate aerosol model lookup tables.

It would be extremely useful to be able to detect the presence of absorbing aerosols from measurements made by the ocean color sensor alone, e.g., to be able to distinguish between absorbing and nonabsorbing aerosols. At present there is no way to effect this; however, computations using Mie scattering suggest that MODIS observations of $\rho_t(\lambda)$ for $\lambda > 865$ nm, may be useful in this regard. Figure 18 compares the $\varepsilon(\lambda, 865)$ for Haze C distributions of nonabsorbing

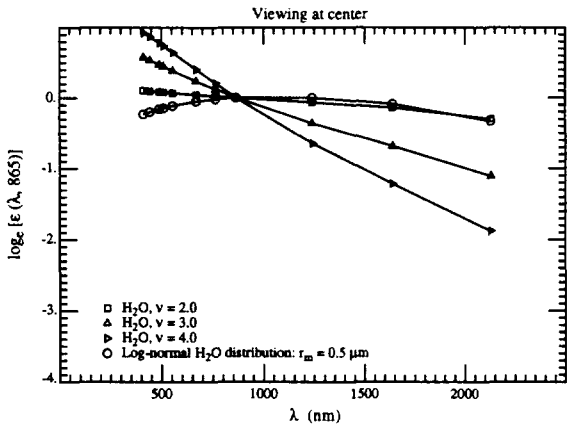

Figure 18a. $\varepsilon(\lambda, 865)$ for nadir viewing with $\theta_0 = 60°$ for the Haze C models composed of liquid water.

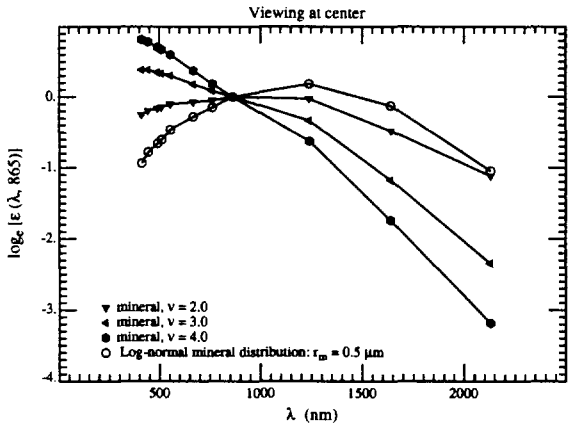

Figure 18b. $\varepsilon(\lambda, 865)$ for nadir viewing with $\theta_0 = 60°$ for the Haze C models composed of absorbing minerals.

(liquid water) and absorbing (minerals transported over the oceans with the index of refraction taken from *d'Almeida, Koepke and Shettle* [1991]) aerosol particles. Also included on Figure 18 are computations for a log-normal distribution suggested in *d'Almeida, Koepke and Shettle* [1991] for minerals transported over large distances to the marine environment. In contrast to nonabsorbing aerosols, the mineral aerosol shows a significant decrease in $\varepsilon(\lambda, 865)$ for $\lambda > 1.26$ μm over that extrapolated from the observed $\varepsilon(765, 865)$ and $\varepsilon(1260, 865)$. This behavior of $\varepsilon(\lambda, 865)$ is apparently due to the rapid decrease in the real part of the mineral refractive index beyond 1260 nm. Notwithstanding the perils of using Mie theory to predict the large-angle scattering for irregularly shaped particles [*Mishchenko and Travis*, 1994; *Mugnai and Wiscombe*, 1989] these computations suggest that it may be reasonable to try to use the short-wave infrared (SWIR) bands on MODIS to differentiate between some types of absorbing and nonabsorbing aerosols. Characteristics of these MODIS bands are provided in Appendix B, where it is shown that these

bands on MODIS have sufficient sensitivity (if pixel averaging is employed) to attempt such a differentiation.

4.3 Stratospheric aerosols

In some situations, e.g., following volcanic eruptions or when there are thin cirrus clouds present, there can be significant quantities of aerosol in the stratosphere. *Gordon and Castaño* [1988] showed that the presence of the El Chichón aerosol [*King, Harshvardhan and Arking*, 1984] had little effect on CZCS atmospheric correction; however, at the higher correction accuracy required for MODIS the *Gordon and Wang* [1994a] algorithm may be degraded by the presence of stratospheric aerosol. Although not listed in Table 1, MODIS is equipped with a spectral band at 1380 nm that can be used to assess the contamination of the imagery by stratospheric aerosol (Appendix B). This spectral band is centered on a strong water vapor absorption band and photons penetrating through the stratosphere will usually be absorbed by water vapor in the free troposphere [*Gao, Goetz and Wiscombe*, 1993]. Thus, any radiance measured at 1.38 μm can, in the first approximation, be assumed to be scattered by the stratospheric aerosol alone, providing a mechanism for estimating the stratospheric contribution.

The author and coworkers are engaged in assessing the effect of stratospheric aerosols on atmospheric correction and studying ways in which to correct the contamination, assuming that all radiance detected at 1380 nm results from scattering by the stratospheric aerosol *alone*. Briefly, the stratospheric aerosol contributes to the reflectance at all wavelengths. Thus, in its presence the total reflectance will be changed by an amount $\delta\rho_t^{(s)}$, i.e.,

$$\rho_t^{(s)}(\lambda) = \rho_t(\lambda) + \delta\rho_t^{(s)}(\lambda),$$

where $\rho_t^{(s)}$ is the reflectance of the entire ocean-atmosphere system in the presence of stratospheric aerosol, and ρ_t the reflectance in its absence. To assess the impact of the stratospheric aerosol, the multiple-scattering algorithm was operated using simulated values of $\rho_t^{(s)}(\lambda)$ in the place of $\rho_t(\lambda)$, for four stratospheric aerosol types. The preliminary results suggest that stratospheric aerosol/cirrus cloud contamination does not seriously degrade the *Gordon and Wang* [1994a] algorithm except for large ($\sim$ 60°) solar zenith angles and large ($\sim$ 45°) viewing angles, for which multiple scattering effects can be expected to be particularly severe.

The performance of a hierarchy of algorithms for using the 1380 nm MODIS band to correct for stratospheric aerosol/cirrus clouds, are also being examined. The approach is to use $\rho_t^{(s)}(1380)$ to estimate $\delta\rho_t^{(s)}(\lambda)$ in the visible and NIR. The procedures being investigated range from from simply subtracting the reflectance at 1380 nm from that in the visible bands, i.e., $\delta\rho_t^{(s)}(\lambda) = \rho_t^{(s)}(1380)$, to assuming all of the optical properties of the stratospheric aerosol are known (measurement at 1380 nm providing the concentration) and carrying out multiple scattering computations to estimate $\delta\rho_t^{(s)}(\lambda)$. It is not surprising that the most complex procedures yield the best results; however, it is surprising that the complex procedures appear to only reduce the error in the retrieved water-leaving radiance by $\lesssim$ a factor of two compared to the simplest procedures.

4.4 Residual instrument polarization

All scanning radiometers display some sensitivity to the polarization of the radiance they are intended to measure. For MODIS, it was specified that this polarization sensitivity should be less than 2%, and that it be mapped as part of the sensor characterization procedure. Depending on how well the MODIS meets this specification, a correction may be required to remove the residual polarization effects from ρ_t. We have developed a formalism [*Gordon*, 1988] which provides the framework for removal of instrumental polarization-sensitivity effects. The difficulty with removing the polarization sensitivity error is that the polarization properties of the radiance backscattered by the aerosol are unknown. Although the details of the correction process have yet to determined, simulations of this effect for an instrument possessing $\sim$ 3–4 times the polarization sensitivity expected for MODIS are presently being carried out. Preliminary results suggest that elimination of the polarization effect is possible at the required level of accuracy by estimating the polarization of the top-of-atmosphere radiance to be that expected for a pure Rayleigh scattering atmosphere. This is understandable in the blue, where Rayleigh scattering is the principal contributor to ρ_t.

4.5 In-water radiance distribution

Algorithms for retrieving total pigments, chlorophyll, etc., from ocean color imagery are developed by relating the nadir-viewing water-leaving radiance to the quantity in question. In the analysis of ocean color imagery it has always been assumed that $[\rho_w]_N$ is independent of the

viewing angle. This assumption was based on a small number of observations, e.g., see *Smith* [1974] and references therein, which suggests that $L_u(z, \theta, \phi)$, the upwelling radiance at depth z beneath the surface and traveling in a direction specified by the angles (θ, ϕ), is only weakly dependent on θ and ϕ. However, in a series of papers Morel and Gentili [*Morel and Gentili*, 1991; *Morel and Gentili*, 1993; *Morel and Gentili*, 1996] studied theoretically the bidirectional effects as a function of the sun-viewing geometry and the pigment concentration. Their simulations suggest that, although the bidirectional effects nearly cancel in the estimation of the pigment concentration using radiance ratios (Eq. (4)), $L_u(z, \theta, \phi)$ can depend significantly on θ, ϕ and θ_0. This means that the value of $[\rho_w]_N$ retrieved in atmospheric correction is actually appropriate only to the viewing direction in which the measurement of ρ_t is made. Since most in-water algorithms have been developed based on nadir-viewing measurements, the derived $[\rho_w]_N$ values should be corrected to nadir-viewing geometry. This requires understanding the bidirectional effects. This is effected by direct determination of the upwelling radiance distribution for a variety of waters and solar zenith angles using an electro-optics radiance camera system developed by *Voss* [1989], e.g., see *Morel, Voss and Gentili* [1995]. These measurements will provide direct determination of the effect, and will yield an algorithm for extrapolation to the nadir viewing direction as required for derived product algorithms.

4.6 Diffuse transmittance

The diffuse transmittance was mentioned in Section 2. It is defined as the water-leaving radiance in a particular viewing direction (θ_v, ϕ_v) "transmitted" to the top of the atmosphere, i.e.,

$$t(\theta_v, \phi_v) = \frac{\rho_w(\theta_v, \phi_v)_{\mathrm{Top}}}{\rho_w(\theta_v, \phi_v)}.$$

Thus, if the atmosphere were only illuminated from below with radiance $\rho_w(\theta, \phi)$, the radiance measured at the top of the atmosphere in the direction (θ_v, ϕ_v) would be $t(\theta_v, \phi_v)\rho_w(\theta_v, \phi_v)$. The diffuse transmittance accounts for the direct loss from $\rho_w(\theta_v, \phi_v)$ due to absorption and scattering within the atmosphere, as well as for the gain in radiance in the direction (θ_v, ϕ_v) due to scattering of $\rho_w(\theta, \phi)$, i.e., from all other upward directions, into (θ_v, ϕ_v). In the case of the CZCS, it was assumed that $\rho_w(\theta, \phi)$ is independent of (θ, ϕ). Then, $t(\theta_v, \phi_v, \lambda)$ was approximated by [*Gordon et al.*, 1983]

$$t(\theta_v, \phi_v, \lambda) = \exp\Big[-\left(\frac{\tau_r(\lambda)}{2} + \tau_{Oz}(\lambda)\right)\left(\frac{1}{\mu_v}\right)\Big] t_a(\theta_v, \lambda), \tag{16}$$

where

$$t_a(\theta_v, \lambda) = \exp\Big[-\frac{[1 - \omega_a(\lambda)F_a(\mu_v, \lambda)]\tau_a(\lambda)}{\mu_v}\Big], \tag{17}$$

and $\mu_v = \cos\theta_v$. $F_a(\mu_v, \lambda)$ is related to the scattering phase function of the aerosol and is given by

$$F_a(\mu_v, \lambda) = \frac{1}{4\pi}\int_0^1 P_a(\alpha, \lambda)\, d\mu\, d\phi,$$

where $P_a(\alpha, \lambda)$ is the aerosol phase function at λ (normalized to 4π) for a scattering angle α, and

$$\cos\alpha = \mu\mu_v + \sqrt{(1-\mu^2)(1-\mu_v^2)}\cos\phi.$$

If θ_v is $\lesssim 60°$ the factor $[1 - \omega_a(\lambda)F_a(\mu_v, \lambda)]$ is usually $\ll 1$, so t_a depends only weakly on the aerosol optical thickness and was taken to be unity for CZCS.

As retrieval of ρ_w from ρ_t requires t, and relative error in t will yield an equivalent relative error in ρ_w, it is important to compute this quantity as accurately as possible. Because the correction algorithm provides models of the aerosol, it is possible to incorporate all of the multiple scattering and aerosol effects into t in the form of look up tables, and considerably improve its accuracy. Unfortunately, any precomputed t must be based on an assumed form for the water-leaving radiance distribution. The natural distribution to assume is uniform (independent of direction); however, as described in Subsection 4.5, $L_u(\theta, \phi)$ just beneath the surface is not uniform, so this assumption cannot be correct. In fact, the appropriate transmittance to use to propagate the water-leaving reflectance to the top of the atmosphere depends on the actual variation of $L_u(\theta, \phi)$ with θ and ϕ. The extent of the effect of $L_u(\theta, \phi)$ on the transmittance is being studied [*Yang and Gordon*, in preparation], and preliminary results indicate that the difference between a uniform (subsurface) upwelling distribution and a more-realistic $L_u(\theta, \phi)$ is usually $< 5\%$ of t. This suggests that derivation of $\rho_w(443)$ within $\pm 5\%$ may require knowing, or estimating, the shape of the subsurface radiance distribution. *Morel and Gentili* [1996] have devised an iterative scheme for estimating the shape of the subsurface radiance distribution from an estimate of the pigment concentration. Such a scheme may be required to provide a more realistic value for t.

4.7 Sensor calibration

Since the desired water-leaving reflectance is only a small part of ρ_t, at most $\sim 10 - 15\%$ (Table 1), accurate calibration of the sensor is critical [*Gordon*, 1987]. In this section we describe simulations to estimate the magnitude of the effect of the radiometric calibration error, and discuss how accurate on-orbit calibration can be effected.

To assess the effect of calibration errors, we add a small error to each of the measured reflectances, i.e.,

$$\rho_t'(\lambda) = \rho_t(\lambda)[1 + \alpha(\lambda)], \tag{18}$$

where $\alpha(\lambda)$ is the fractional error in $\rho_t(\lambda)$ and $\rho_t'(\lambda)$ is the value of $\rho_t(\lambda)$ that the incorrect sensor calibration would indicate. The atmospheric correction algorithm is then operated by inserting $\rho_t'(\lambda)$ as the measured value rather than the true value $\rho_t(\lambda)$ and $t\Delta\rho_w \equiv \Delta\rho$ is computed as before.

Assuming the single-scattering algorithm, Eq. (12), is exact, and $\varepsilon(\lambda_i, \lambda_l) = \exp[c(\lambda_l - \lambda_i)]$, it is easy to show that to first order in $\alpha(\lambda)$, the error in the retrieved ρ_w is

$$\begin{aligned} t(\lambda_i)\Delta\rho_w(\lambda_i) = {} & \alpha(\lambda_i)\rho_t(\lambda_i) - \varepsilon(\lambda_i, \lambda_l)\alpha(\lambda_l)\rho_t(\lambda_l) \\ & - \left(\frac{\lambda_l - \lambda_i}{\lambda_l - \lambda_s}\right)\left[\frac{\varepsilon(\lambda_i, \lambda_l)}{\varepsilon(\lambda_s, \lambda_l)}\alpha(\lambda_s)\rho_t(\lambda_s) - \varepsilon(\lambda_i, \lambda_l)\alpha(\lambda_l)\rho_t(\lambda_l)\right] \end{aligned} \tag{19}$$

The first term represents the direct effect of calibration error at λ_i on $\rho_w(\lambda_i)$, while the remaining terms represent the indirect effect from calibration error in the atmospheric correction bands at λ_s and λ_l. The second term obviously increases in importance as λ_i decreases. Note that if all of the spectral bands have calibration error with the same sign, i.e., all $\alpha(\lambda)$ have the same sign, significant cancelation of the atmospheric correction contribution can occur; however, if $\alpha(\lambda_s)$ and $\alpha(\lambda_l)$ have different signs, the error is magnified as the last two terms in Eq. (19) will add.

To see if this holds for the multiple-scattering algorithm as well, it was also operated by inserting $\rho_t'(\lambda)$ as the measured value rather than the true value $\rho_t(\lambda)$. The results of this exercise are presented in Figures 19a–19d for the M80 aerosol model at the center of the scan. In Figures 19a and 19b, $\alpha(765) = \alpha(865)$ with $\alpha(443) = 0$ (Figure 19a) or with $\alpha(443) = \alpha(765) = \alpha(865)$ (Figure 19b). Figures 19a and 19b show the effect of a calibration bias that is the same at 765 and 865 nm. Figures 19c and 19d show the effect of having calibration errors that are of opposite

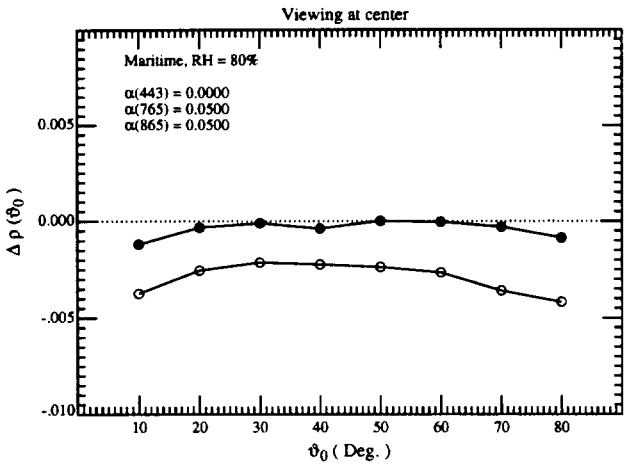

Figure 19a. Error in the retrieved $t(443)\rho_w(443)$ for viewing at the center of the scan with a Maritime aerosol at RH = 80% as a function of the solar zenith angle with $\tau_a(865) = 0.2$ and calibration errors $\alpha(443)$, $\alpha(765)$, and $\alpha(865)$ in Eq. (18) (open circles). Solid circles are for $\alpha(\lambda_i) = 0$ for all λ_i.

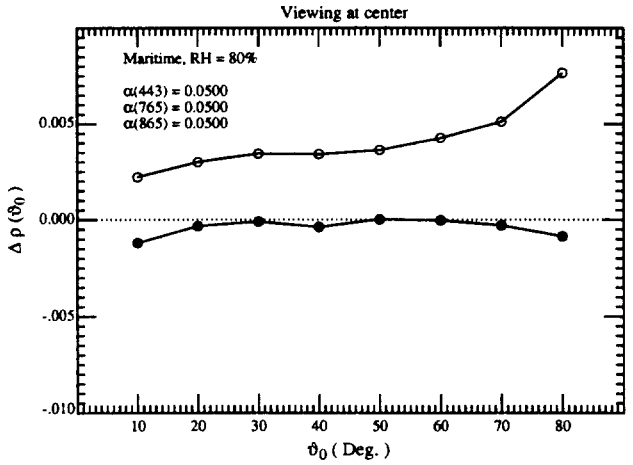

Figure 19b. Error in the retrieved $t(443)\rho_w(443)$ for viewing at the center of the scan with a Maritime aerosol at RH = 80% as a function of the solar zenith angle with $\tau_a(865) = 0.2$ and calibration errors $\alpha(443)$, $\alpha(765)$, and $\alpha(865)$ in Eq. (18) (open circles). Solid circles are for $\alpha(\lambda_i) = 0$ for all λ_i.

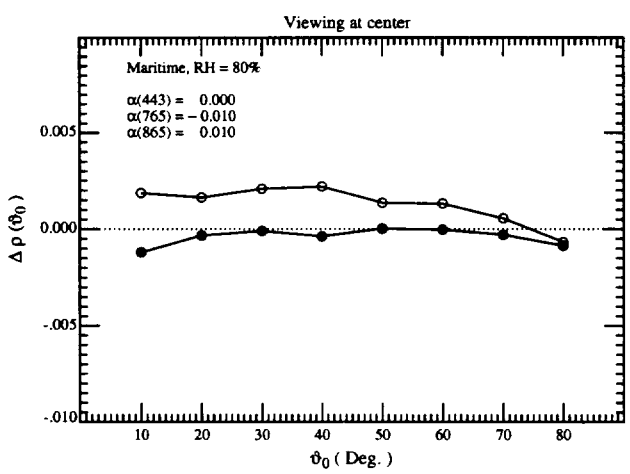

Figure 19c. Error in the retrieved $t(443)\rho_w(443)$ for viewing at the center of the scan with a Maritime aerosol at RH = 80% as a function of the solar zenith angle with $\tau_a(865) = 0.2$ and calibration errors $\alpha(443)$, $\alpha(765)$, and $\alpha(865)$ in Eq. (18) (open circles). Solid circles are for $\alpha(\lambda_i) = 0$ for all λ_i.

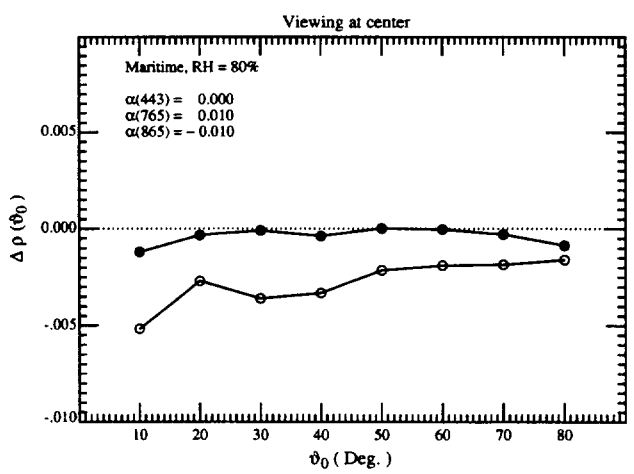

Figure 19d. Error in the retrieved $t(443)\rho_w(443)$ for viewing at the center of the scan with a Maritime aerosol at RH = 80% as a function of the solar zenith angle with $\tau_a(865) = 0.2$ and calibration errors $\alpha(443)$, $\alpha(765)$, and $\alpha(865)$ in Eq. (18) (open circles). Solid circles are for $\alpha(\lambda_i) = 0$ for all λ_i.

sign at 765 and 865 nm. Note that in this case even a small calibration error (1%) can make as significant an error in $\rho_w(443)$ as a large calibration error (5%) when the signs are all the same. As discussed above, the reason the error is so much larger when it is of opposite sign at 765 and 865 nm is that it will cause a large error in the estimated value of $\varepsilon(765, 865)$, and this will propagate through the algorithm causing a large error in the retrieved water-leaving reflectance at 443 nm. In the cases examined in Figure 19, the magnitude of the errors is in quantitative agreement with that predicted by Eq. (19).

As the goal for the calibration of the relevant ocean color bands on MODIS is that L_t have an uncertainty of $< \pm 5\%$, and Figures 19c and 19d show that such an error (even if it were the same in each band) would cause the error in the retrieved $\rho_w(443)$ to be outside the acceptable range. Thus some on-orbit calibration may be required. This is usually termed vicarious calibration [*Evans and Gordon*, 1994; *Fraser and Kaufman*, 1986; *Gordon*, 1987; *Koepke*, 1982; *Slater et al.*, 1987]. It involves making surface measurements of sky radiance, τ_a, ρ_w, etc. to predict ρ_t within a given uncertainty. It is a very attractive method of calibration as the sensor is calibrated in the precise configuration in which it is used. Using the algorithm developed by *Wang and Gordon* [1993] for inverting measurements of sky radiance and τ_a, *Gordon and Zhang* [1996] have shown that with a perfectly calibrated radiometer (to measure the sky radiance) it should be possible to estimate ρ_t with an uncertainty $\sim$ 1–2% in the NIR. This uncertainty combined with an uncertainty of the order of 2–3% in radiometer calibration would mean that $\rho_t(865)$ could be estimated with an uncertainty of $\lesssim 3.5\%$. Thus, in the NIR it should be possible to improve on the 5% uncertainty of MODIS using such surface measurements.

Having achieved this accuracy in the NIR, it is a relatively simple matter to extend this calibration with even higher accuracy to the visible, because there, proportionately more of ρ_t is due to Rayleigh scattering, which is known. Although a complete analysis will be published elsewhere, the basic idea can be seen from the single-scattering approximation. For example, assume that it is desired to estimate ρ_t at 443 nm. First, measurements of $\tau_a(443)/\tau_a(865)$ are made at the surface calibration site. Then Figure 20 provides examples showing the existence of a rough relationship between $\tau_a(443)/\tau_a(865)$ and $\varepsilon(443, 865)$ for all of the aerosol models used in the present work. Such models provide a prediction of $\varepsilon(443, 865)$. Finally, surface measurements of $\rho_w(443)$ are combined with $\rho_r(443)$ to estimate $\rho_{as}(443)$, and thus, the MODIS-derived $\varepsilon(443, 865)$. These two estimates are brought into agreement by adjusting the sensor calibration

at 443 nm. As $\varepsilon(\lambda_i, \lambda_l)$ must be a smooth function of λ_i (Figure 3), it is easy to see that with this procedure, the residual error in all of the spectral bands considered will have the same sign.

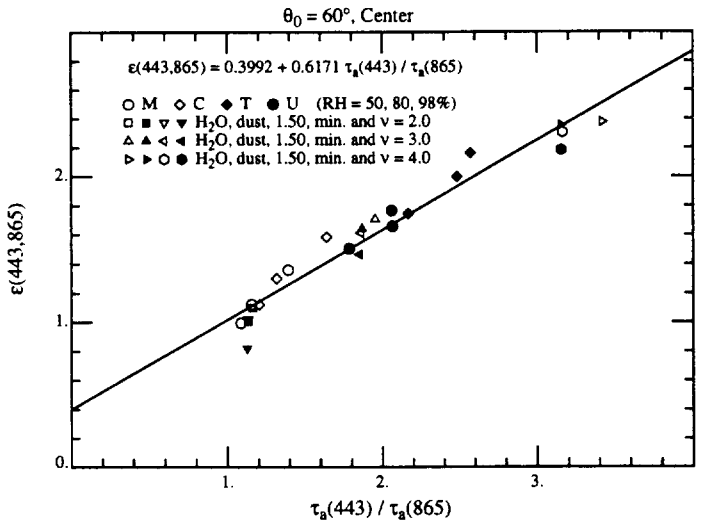

Figure 20. Relationship between $\tau_a(443)/\tau_a(865)$ and $\varepsilon(443, 865)$ at the scan center with $\theta_0 = 60°$ for all of the test aerosol models used in this study.

5. An alternate approach for MISR

The Multiangle Imaging Spectroradiometer [*Diner et al.*, 1989; *Diner et al.*, 1991] (MISR) is scheduled to be flown on the first platform of EOS. MISR consists of a set of nine cameras that view the Earth at nine angles (0, ±26.1°, ±45.6°, ±60.0°, and ±70.5°) to the Earth's surface normal, where positive and negative angles refer to directions ahead of and behind the spacecraft, respectively, and in four spectral bands (Table 1). Thus, MISR will measure the radiance exiting the top of the atmosphere in nine directions at four wavelengths. MISR has a spatial resolution of approximately 250 m at nadir, and if the spatial resolution is degraded by a factor of four to 1 km, it will have sufficient sensitivity to be useful for ocean color observations.

It is easy to adapt the MODIS/SeaWiFS algorithm for use with MISR. In the open ocean, the water-leaving reflectance at 670 nm is very small (Table 1) and can be assumed to be zero

unless the pigment concentration is too large ($\gtrsim 0.5 - 1$ mg/m^3). Thus, one can effect an atmospheric correction using the 670 and 865 nm bands of MISR instead of the 750 (765) and 865 nm bands of MODIS (SeaWiFS).

Alternatively, *Wang and Gordon* [1994c] and *Wang and Gordon* [1994a] describe algorithms for deducing the aerosol optical properties and concentration over the oceans from MISR data. Their algorithms involve comparing the angular distribution of radiance leaving the top of the atmosphere at 865 nm with the predictions of aerosol models. The model that best matches the angular distribution is used to estimate the aerosol properties. The MISR-NIR band is chosen for the retrievals because the water-leaving reflectance can be assumed to be zero there except in the most turbid waters. As the *Wang and Gordon* [1994c] algorithm provides an aerosol model from a set of candidates, it seems reasonable to try to use the chosen candidate model to provide an atmospheric correction in the visible. This method is more attractive than the two-band MODIS/SeaWiFS method, as only a single spectral band (865 nm) is required, i.e., it is not necessary to assume a pigment concentration $\lesssim 0.5 - 1$ mg/m^3.

These two methods of atmospheric correction of the MISR blue band (443 nm) are compared in Table 3. As in *Wang and Gordon* [1994c] we examined two geometries: June 21 with MISR positioned at 30° latitude ($\theta_0 = 20°$, $\phi_v - \phi_0 = 83°, 97°$) called "summer," and Dec. 21 with MISR positioned at 34° latitude ($\theta_0 = 60°$, $\phi_v - \phi_0 = 23°$ and 157°) referred to as "winter." The aerosol model used in generating the pseudo data used to prepare Table 3 was the C80 model with $\tau_a(865) = 0.2$. For MISR, the atmospheric correction was applied to the nadir-viewing camera, and for MODIS the correction was at the scan center (also nadir-viewing). Note that in the Summer geometry, there is little difference between the two atmospheric correction methods, while in the Winter geometry, the MODIS correction is significantly better than the MISR single-band correction; however, even in this case, the MISR correction technique still yields acceptable results.

The test provided in Table 3 suggests that it is possible to atmospherically correct MISR imagery using a single spectral band. This could be of significant value for imagery obtained in coastal zones and large inland lakes. Near the coast, the water is often turbid due to sediments introduced runoff from the land or resuspended from the bottom. The reflectance of such waters generally decreases as the wavelength increases from the green to red to the NIR due to the in-

Table 3: Comparison between performance of the MISR and MODIS (SeaWiFS) atmospheric correction techniques applied to MISR data. The tabulated quantity is $\Delta\rho \equiv t\Delta\rho_w(443)$.

(a) Summer Geometry

Instrument	443 nm	555 nm
MODIS	$+\ 3.02 \times 10^{-4}$	$+\ 1.03 \times 10^{-4}$
MISR	$-\ 2.02 \times 10^{-4}$	$-\ 0.63 \times 10^{-4}$

(b) Winter Geometry

Instrument	443 nm	555 nm
MODIS	$+\ 3.42 \times 10^{-4}$	$+\ 0.65 \times 10^{-4}$
MISR	-10.01×10^{-4}	$-\ 9.53 \times 10^{-4}$

creasing absorption with increasing wavelength by the water itself; however, for such waters, it is often not possible to assume $\rho_w \approx 0$ at 670 nm or even 750 nm; however, as long as $\rho_w \approx 0$ at 865 nm, a single-band MISR correction could be made. As the reflectance of coastal waters is generally larger than the open ocean, the accuracy of the atmospheric correction need not be as great as in the open ocean to obtain $\rho_w(443)$ within $\pm 5\%$. In such turbid coastal waters it also appears possible to atmospherically correct MODIS using MISR in the following manner: (1) the MISR aerosol algorithm is used to provide the candidate aerosol model for MODIS; and (2) the MODIS 865 nm band is used along with the candidate aerosol model to correct the other MODIS bands. Finally, combining the wide spectral coverage of MODIS (412 to 2130 nm) and the wide range of viewing angles of MISR may be of considerable value in identifying the presence of absorbing aerosols. Such synergism between MODIS and MISR is only possible because they share the same platform.

6. Concluding remarks

In this paper we have described the atmospheric correction algorithms proposed for SeaWiFS, MODIS, and MISR, and simulated their performance for a variety of aerosol types and concentrations. In addition we have examined the effects of the simplifying assumptions used in the

original development of the algorithm, and examined several remaining issues. One goal of the paper was to try to provide a better understanding of the nature of the weaknesses of the basic algorithm, in order to develop plans for resolving inadequacies. Several conclusions can be made on the basis of the work presented in this paper.

First, considering the fact that the maritime atmosphere, far from the influence land and/or anthropogenic aerosol sources, is very clear, the single-scattering algorithm should be sufficient over most of the open ocean. Since the multiple-scattering algorithm reduces to the single-scattering algorithm in the limit of small $\tau_a(865)$, one expects that this algorithm should also provide an adequate correction in such cases. However, this will only obtain as long as the candidate aerosol models encompass the range of variability of the actual maritime aerosol.

Second, the multiple-scattering algorithm is capable of providing an adequate correction for higher aerosol optical thicknesses, but again, this requires a realistic set of candidate aerosol models. If the aerosols absorb significantly, e.g., the aerosol over the Middle Atlantic Bight during summer air pollution incidents or the dust transported by the winds from Africa over the Tropical North Atlantic, it is absolutely necessary to restrict the candidate aerosol set to include only members that have the proper absorption characteristics. Since proper sets may be appropriate only for a restricted regions, an accurate aerosol climatology will be necessary to correct imagery in regions other than the open ocean. Such a climatology does not exist at present; however, efforts by several research groups are underway to build one.

Third, absorbing aerosols present an additional difficulty. In the case of nonabsorbing aerosols, given a realistic set of candidate aerosol models, the multiple-scattering algorithm is shown through simulations to be insensitive to the vertical structure of the aerosol. Thus, multiple-scattering lookup tables prepared by solving the radiative transfer equations for a two-layer atmosphere, with the aerosols in the lower layer, are adequate for weakly- or nonabsorbing aerosols. In contrast when the aerosol shows significant absorption, the multiple-scattering algorithm was shown to be very sensitive to the physical thickness of the aerosol layer, even if an appropriate set of candidate aerosol models are employed. This implies that expected layer thickness must be included in the aerosol climatology discussed above.

Fourth, the effects of the simplifying assumptions used in the development of the algorithm, such as approximating the atmosphere by a plane-parallel medium, ignoring polarization of the

light field in the simulation of ρ_t, and assuming that the sea surface was smooth, were shown to have been justified to the extent that they introduce little error in the resulting atmospheric correction.

Fifth, the influence of whitecaps was shown to be dependent on the spectral properties of their reflectance, i.e., on whether whitecap reflectance is similar to that measured in the surf zone and significantly smaller in the NIR than in the visible. Thus, effort must be made to understand the spectral reflectance of whitecaps and its relationship to wind speed.

Sixth, other issues such as the appropriateness of candidate aerosol models, stratospheric aerosols, the effect of residual instrument polarization sensitivity, the variability of the in-water radiance distribution and its influence on the diffuse transmittance of the atmosphere, and the assessment of, and correction for, error in the sensor calibration are all under study.

A new atmospheric correction technique, which requires the water-leaving reflectance to be negligible in only a *single* spectral band rather than *two* spectral bands, was developed and applied to simulated MISR data. It was shown that for certain geometries this single-band algorithm produced ρ_w retrievals that were as good as the MODIS-type algorithm based on assuming $\rho_w = 0$ at both 670 and 865 nm. This raises the possibility of synergistically using MISR imagery to provide the proper candidate aerosol model for correcting MODIS imagery in the coastal zone, and to help in identifying absorbing aerosols. Application of such a technique to these EOS sensors would probably require the availability of Level 1 data (calibrated and geometrically-located radiances) at a single processing center.

Finally, based on the simulations presented here, atmospheric correction appears to be limited principally by our ability to correctly predict the reflectivity enhancement of whitecaps, and by the representativeness of the aerosol climatology (particularly in regions with strongly-absorbing aerosols) that must be developed and used in the multiple-scattering algorithm. However, it should be recognized that much of the difficulty associated with the algorithm (absorbing aerosols) applies to a relatively small (although important) portion of the ocean. Except for the whitecap limitation, there will be little difficulty atmospherically correcting most of the imagery from EOS ocean color sensors. Given their improved radiometric sensitivity, wider spectral range, and radiometric calibration stability compared to CZCS, a concomitant increase in the accuracy and stability of the derived products will be realized.

7. Appendices

Appendix A. The sun glitter masking algorithm

In this appendix we provide the equations required to prepare a mask to flag pixels that are seriously contaminated by sun glitter. The intention is that the sun glitter mask be applied to the imagery prior to the application of the normalized water-leaving radiance retrieval algorithm described in the text.

The contribution to the measured radiance at the top of the atmosphere from sun glitter — the specular reflection of sunlight from the sea surface and propagation to the sensor — is based on the formulation of *Cox and Munk* [1954]. In this development the sea surface is modeled as

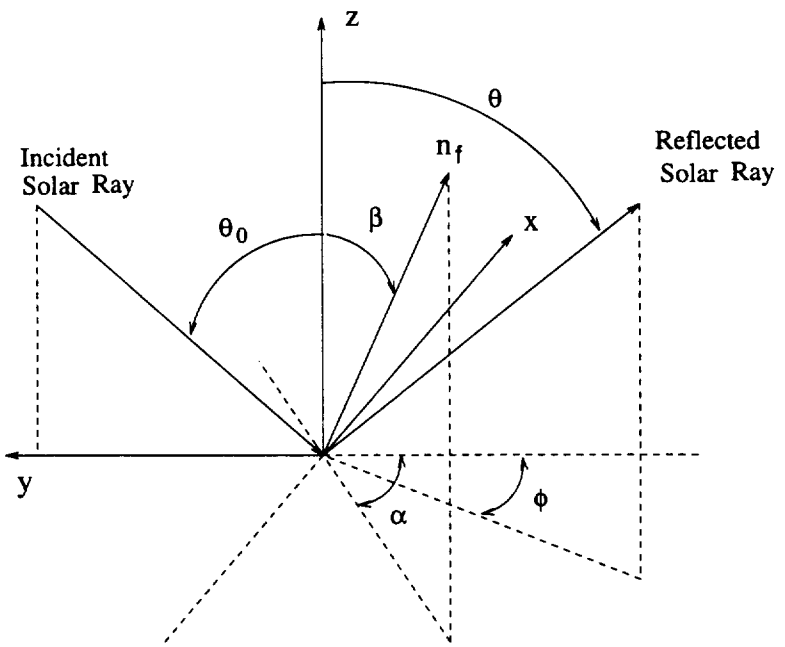

Figure 21. Geometry of reflection from a rough sea surface. n_f is the unit normal to the facet that is oriented properly to reflect the sunlight as shown.

a collection of facets with individual slope components z_x and z_y. In a coordinate system with the $+y$ axis pointing toward the sun (projection of the sun's rays on the sea surface is along the $-y$ axis), given the solar zenith angle and the angles θ and ϕ specifying the reflected ray, the orientation (β, α) of the facet normal n_f (Figure 21) required for a facet to reflect sunlight in the

direction of (θ, ϕ) is found from the following equations

$$\cos(2\omega) = \cos\theta\cos\theta_0 - \sin\theta\sin\theta_0\cos\phi$$

$$\cos\beta = (\cos\theta + \cos\theta_0)/2\cos\omega$$

$$\cos\alpha = (\cos\phi\cos\theta - \sin\theta)/2\cos\omega\sin\beta$$

$$\sin\alpha = (\sin\phi\cos\theta)/2\cos\omega\sin\beta$$

$$z_x = \sin\alpha\tan\beta$$

$$z_y = \cos\alpha\tan\beta.$$

Note that for a flat (smooth) surface, $\phi = 0$. Let χ be the the angle between the projection of the sun's rays on the sea surface and the direction of the wind vector $\vec{W}$, i.e., if $\chi = 0$ the wind vector points in the direction of $-y$ in Figure 1. χ is measured positive in a clockwise direction (looking toward the surface), i.e., if $0 < \chi < 90°$, the wind vector is in the quadrant formed by the $-x$ and $-y$ axes. Then, ρ_g is given by

$$\rho_g(\theta, \phi; \theta_0, \phi_0) = \frac{\pi r(\omega)}{4\cos\theta_0\cos\theta\cos^4\beta} p(z'_x, z'_y)$$

where $p(z'_x, z'_y)$ is the probability density of surface slopes given by

$$p(z'_x, z'_y) = (2\pi\sigma_u\sigma_c)^{-1}\exp[-(\xi^2 + \eta^2)/2]\left[1 + \sum_{i=1}^{\infty}\sum_{j=1}^{\infty} c_{ij}H_i(\xi)H_j(\eta)\right],$$

with

$$\xi = z'_x/\sigma_c = \sin\alpha'\tan\beta/\sigma_c$$

$$\eta = z'_y/\sigma_u = \cos\alpha'\tan\beta/\sigma_u$$

$$\alpha' = \alpha - \chi.$$

$r(\omega)$ is the Fresnel reflectance for unpolarized light incident at an angle ω, and H_i is the Hermite polynomial of order i. The constants σ_u, σ_c, and c_{ij} were determined by *Cox and Munk* [1954] by fitting the radiance from glitter patterns photographed from aircraft to these equations. For $\vec{W}$ in m/s, they are

$$\sigma_c^2 = 0.003 + 1.92 \times 10^{-3}\,W \quad \pm 0.002$$

$$\sigma_u^2 = 0.000 + 3.16 \times 10^{-3}\,W \quad \pm 0.004$$

$$c_{21} = 0.01 - 8.6 \times 10^{-3}\,W \quad \pm 0.03$$

$$c_{03} = 0.04 - 33 \times 10^{-3}\,W \quad \pm .012$$

$$c_{40} = 0.40 \quad \pm 0.23$$

$$c_{22} = 0.12 \quad \pm 0.06$$

$$c_{04} = 0.23 \quad \pm 0.41$$

The contribution of ρ_g to the reflectance measured at the top of the atmosphere, $T\rho_g$, where T is the direct transmittance of the atmosphere (Section 2), is just

$$\rho_g \exp\left[-\tau\left(\frac{1}{\cos\theta} + \frac{1}{\cos\theta_0}\right)\right],$$

where τ is the total optical thickness of the atmosphere.

The sun glitter mask uses the wind vector $\vec{W}$ to estimate $T\rho_g$ for each pixel, and if the estimate is larger than a threshold value (to be determined) the pixel is flagged and the normalized water-leaving radiance algorithm is not applied. As the aerosol optical thickness is unknown, the conservative approach is taken to maximize the area masked by choosing $\tau_a = 0$.

Appendix B. The MODIS short-wave infrared bands

In Subsection 4.2 it was suggested that the MODIS SWIR bands may be useful in separating situations dominated by absorbing mineral aerosols from those dominated by nonabsorbing aerosols. In this appendix it is shown that MODIS has sufficient radiometric sensitivity in the SWIR to justify attempting such a separation. The specifications of the MODIS SWIR bands are provided in Table 4 in terms of reflectance for a solar zenith angle of 60°. In the table, $\Delta\rho_{\mathrm{Dig}}$

Table 4: Radiometric performance of MODIS in the SWIR

Band	λ (nm)	ρ_{max} (Sr^{-1})	NE$\Delta\rho$ (Sr^{-1})	$\Delta\rho_{\mathrm{Dig}}$ (Sr^{-1})
5	1240	0.94	6.2×10^{-4}	2.2×10^{-4}
6	1640	1.88	7.2×10^{-4}	4.6×10^{-4}
7	2130	1.50	6.2×10^{-4}	3.6×10^{-4}
26	1380	1.64	7.2×10^{-4}	4.0×10^{-4}

represents the quantization interval of the 12-bit digitized reflectance. Bands 5, 6, and 7 have a spatial resolution of 500 m compared to 1000 m for Bands 8-16 and 26. Comparing NE$\Delta\rho$ and $\Delta\rho_{\mathrm{Dig}}$ suggests that averaging four 500 m pixels to form one 1000 m pixel could reduce the effective NE$\Delta\rho$ by $\sim$ a factor of 2, particularly for Band 5. Averaging larger numbers of 500 m pixels should lead to still lower NE$\Delta\rho$'s.

To estimate the aerosol component of the expected reflectance in these bands, we take a conservative approach. We assume a mineral aerosol (strongly absorbing) with $\tau_a(865) = 0.2$ and use the single scattering approximation with the surface reflection terms omitted. Then for nadir viewing and $\theta_0 = 60°$,

$$\rho_{as}(\lambda) = \frac{\omega_a(\lambda)P_a(120°, \lambda)\tau_a(\lambda)}{2}.$$

For the size distribution we use the Haze C model with $\nu = 2$ (the smallest $P_a(120°)$) as well as the log-normal model described in Subsection 4.2. The resulting values of ρ_{as} are presented in Table 5.

These computations suggest that Bands 5 and 6 would be able to detect aerosols with a signal-to-noise ratio of $\sim$ 20, with pixel averaging. In contrast, it appears that Band 7 would be

useful only at higher $\tau_a(865)$, or by averaging a larger number of pixels. One must note, however, that these estimates for ρ_{as} are conservative.

Table 5: Expected aerosol reflectance in the SWIR.
Values for ρ_{as} and NE$\Delta\rho$ have been multiplied by 10^{+4}.

Band	λ (nm)	ρ_{as} (Sr^{-1})		NE$\Delta\rho$ (Sr^{-1})
		Haze C	Log-normal	
16	865	110	103	0.8
5	1240	106	128	6.2
6	1640	68	94	7.2
7	2130	39	37	6.2

Appendix C. Required ancillary data

There are several sets of ancillary data that are required to operate the $[L_w]_N$ retrieval algorithm. These are listed in Table 6. They may be needed on at most a $1^\circ \times 1^\circ$ latitude-longitude grid, but probably a coarser grid, e.g., $3^\circ \times 3^\circ$ will be sufficient considering the expected quality of some of the data. We will now discuss each ancillary data set required.

Table 6: Required ancillary data.

Quantity	Ancillary Data
$\rho_t(\lambda_i)$	$F_0(\lambda_i)$
$\rho_r(\lambda_i)$	$\tau_{Oz}(\lambda_i)$, W, P_0
$\rho_{wc}(\lambda_i)$	W
$\rho_g(\lambda_i)$	$\vec{W}$
$t(\lambda_i)$	$\tau_{Oz}(\lambda_i)$, P_0
$T(\lambda_i)$	$\tau_{Oz}(\lambda_i)$, P_0, $\tau_a(\lambda_i)$
$\epsilon(\lambda_i, \lambda_j)$	RH

The extraterrestrial solar irradiance is required to convert from L_t to ρ_t. It is planned that this be taken from *Neckel and Labs* [1984] unless newer, more accurate, determinations become available in the future. In the event that MODIS is calibrated in reflectance units directly, this quantity is only needed to convert $[\rho_w]_N$ to the desired $[L_w]_N$.

In the radiative transfer model the atmosphere is assumed to be composed of three layers. The top is the Ozone layer and is nonscattering, the second is a molecular scattering layer and the third is the aerosol layer. The Ozone optical thickness $\tau_{Oz}(\lambda)$ is needed to compute the two way transmittance of ρ_r, ρ_w, ρ_{wc} and ρ_g through the Ozone layer. Since the Ozone absorption is small ($\tau_{Oz} \lesssim 0.035$) high accuracy is not needed. It is estimated that an error in the Ozone concentration of $\sim 20 - 40$ mAtm–cm (Dobson Units) could be tolerated. The source will either be MODIS itself (most convenient) or a sensor on the NOAA system.

The atmospheric pressure is needed to compute the Rayleigh optical thickness required for the computation of ρ_r. This is also used in the transmittances t and T. An error $< \pm 5$ hPa should be sufficient.

The wind speed, if known, is used in the computation of ρ_r, otherwise ρ_r is computed with $W = 0$. It is also required for the estimation of $[\rho_{wc}]_N$. The wind vector is required for the construction of a glint mask, i.e., a mask to remove areas contaminated by sun glint from the imagery before processing (Appendix A). The importance of creating a realistic mask is that good data may be masked if the mask is made in too conservative a manner. An error of $< 1 - 2$ m/s in the speed and $< 30°$ on the direction should be sufficient.

The surface relative humidity (RH) is not really needed by the algorithm; however, it could be useful as a constraint on the candidate aerosol models chosen by the correction algorithm. The error in the value of RH should be $< \pm 5 - 10\%$ to be useful. The source of the data for P_0, $\vec{W}$, and RH will be the output of numerical weather models, probably from NMC.

Acknowledgment

The author wishes to acknowledge the students and postdocs who have contributed to this work: Menghua Wang, Kuiyuan Ding, Tianming Zhang, Fan He, Haoyu Yang, and Tao Du. He is also grateful to Drs. R. Fraser and R. Frouin for providing careful reviews resulting in several improvements of the manuscript. This work received support from the National Aeronautics and Space Administration under Grant NAGW-273 and Contracts NAS5-31363 and NAS5-31743, and the Jet Propulsion Laboratory under Contract 959033.

References

d'Almeida, G. A., P. Koepke and E. P. Shettle, *Atmospheric Aerosols — Global Climatology and Radiative Characteristics*, A. Deepak Publishing, Hampton, VA, 1991.

André, J. -M. and A. Morel, Atmospheric Corrections and Interpretation of Marine Radiances in CZCS Imagery, Revisited, *Oceanologica Acta*, *14*, 3–22, 1991.

Asrar, G. and J. Dozier, *EOS: Science Strategy for the Earth Observing System*, AIP Press, Woodbury, N.Y., 1994, 119 pp.

Bricaud, A. and A. Morel, Atmospheric Corrections and Interpretation of Marine Radiances in CZCS Imagery: Use of a Reflectance Model, *Oceanologica Acta*, *7*, 33–50, 1987.

Clarke, G. L., G. C. Ewing and C. J. Lorenzen, Spectra of Backscattered Light from the Sea Obtained From Aircraft as a Measurement of Chlorophyll Concentration, *Science*, *167*, 1119–1121, 1970.

Cox, C. and W. Munk, Measurements of the Roughness of the Sea Surface from Photographs of the Sun's Glitter, *Jour. Opt. Soc. of Am.*, *44*, 838–850, 1954.

Deirmendjian, D., *Electromagnetic Scattering on Spherical Polydispersions*, Elsevier, New York, NY, 1969, 290 pp.

Deschamps, P. Y., M. Herman and D. Tanre, Modeling of the atmospheric effects and its application to the remote sensing of ocean color, *Applied Optics*, *22*, 3751–3758, 1983.

Diner, D. J., C. J. Bruegge, J. V. Martonchik, T. P. Ackerman, R. Davies, S. A. W. Gerstl, H. R. Gordon, P. J. Sellers, J. Clark, J. A. Daniels, E. D. Danielson, V. G. Duval, K. P. Klaasen, G. W. L. A. D. I. Nakamoto, R. Pagano and T. H. Reilly, MISR: A Multi-angle Imaging SpectroRadiometer for Geophysical and Climatological Research from EOS, *IEEE Transactions on Geoscience and Remote Sensing*, *27*, 200–214, 1989.

Diner, D. J., C. J. Bruegge, J. V. Martonchik, G. W. Bothwell, E. D. Danielson, E. L. Floyd, V. G. Ford, L. E. Hovland, K. L. Jones and M. L. White, A Multi-angle Imaging SpectroRadiometer for Terrestrial Remote Sensing from the Earth Observing System, *International Journal of Imaging Systems and Technology*, *3*, 92–107, 1991.

Ding, K. and H. R. Gordon, Atmospheric correction of ocean color sensors: Effects of earth curvature, *Applied Optics*, *33*, 7096–7016, 1994.

Ding, K. and H. R. Gordon, Analysis of the influence of O_2 *A*-band absorption on atmospheric correction of ocean color imagery, *Applied Optics*, *34*, 2068–2080, 1995.

Eldridge, R. G., Water Vapor Absorption of Visible and Near Infrared Radiation, *Applied Optics*, *4*, 709–713, 1967.

Evans, R. H. and H. R. Gordon, CZCS 'System Calibration:' A retrospective examination, *Jour. Geophys. Res.*, *99C*, 7293–7307, 1994.

Feldman, G. C., N. Kuring, C. Ng, W. Esaias, C. R. McClain, J. Elrod, N. Maynard, D. Endres, R. Evans, J. Brown, S. Walsh, M. Carle and G. Podesta, Ocean Color: Availability of the Global Data Set, *EOS Trans. Amer. Geophys. Union*, *70*, 634–641, 1989.

Fraser, R. S., Degree of Interdependence among Atmospheric Optical Thickness in Spectral Bands between 0.36 and 2.4 μm, *Applied Optics*, *14*, 1187–1196, 1975.

Fraser, R. S. and Y. J. Kaufman, Calibration of satellite sensors after launch, *Applied Optics*, *25*, 1177–1185, 1986.

Frouin, R., M. Schwindling and P. Y. Deschamps, 1995, Spectral reflectance of sea foam in the visible and near-infrared: In-situ measurements and implications for remote sensing of ocean color and aerosols, *Jour. Geophys. Res.*, (In press).

Gao, B. -C., A. F. H. Goetz and W. J. Wiscombe, Cirrus cloud detection from airborne imaging spectrometer data using the 1.38 micron water vapor band, *Geophysical Research Letters*, *20*, 301–304, 1993.

Gordon, H. R., Radiative Transfer: A Technique for Simulating the Ocean in Satellite Remote Sensing Calculations, *Applied Optics*, *15*, 1974–1979, 1976.

Gordon, H. R., Removal of Atmospheric Effects from Satellite Imagery of the Oceans, *Applied Optics*, *17*, 1631–1636, 1978.

Gordon, H. R., Calibration Requirements and Methodology for Remote Sensors Viewing the Oceans in the Visible, *Remote Sensing of Environment*, *22*, 103–126, 1987.

Gordon, H. R., Ocean Color Remote Sensing Systems: Radiometric Requirements, *Society of Photo-Optical Instrumentation Engineers, Recent Advances in Sensors, Radiometry, and Data Processing for Remote Sensing*, *924*, 151–167, 1988.

Gordon, H. R., Radiometric Considerations for Ocean Color Remote Sensors, *Applied Optics*, *29*, 3228–3236, 1990.

Gordon, H. R., J. W. Brown and R. H. Evans, Exact Rayleigh Scattering Calculations for use with the Nimbus-7 Coastal Zone Color Scanner, *Applied Optics*, *27*, 862–871, 1988.

Gordon, H. R., O. B. Brown, R. H. Evans, J. W. Brown, R. C. Smith, K. S. Baker and D. K. Clark, A Semi-Analytic Radiance Model of Ocean Color, *Jour. Geophys. Res.*, *93D*, 10909–10924, 1988.

Gordon, H. R. and D. J. Castaño, The Coastal Zone Color Scanner Atmospheric Correction Algorithm: Multiple Scattering Effects, *Applied Optics*, *26*, 2111–2122, 1987.

Gordon, H. R. and D. J. Castaño, The Coastal Zone Color Scanner Atmospheric Correction Algorithm: Influence of El Chichón, *Applied Optics*, *27*, 3319–3321, 1988.

Gordon, H. R. and D. K. Clark, Atmospheric effects in the remote sensing of phytoplankton pigments, *Boundary-Layer Meteorology*, *18*, 299–313, 1980.

Gordon, H. R. and D. K. Clark, Clear water radiances for atmospheric correction of coastal zone color scanner imagery, *Applied Optics*, *20*, 4175–4180, 1981.

Gordon, H. R., D. K. Clark, J. W. Brown, O. B. Brown, R. H. Evans and W. W. Broenkow, Phytoplankton pigment concentrations in the Middle Atlantic Bight: comparison between ship determinations and Coastal Zone Color Scanner estimates, *Applied Optics*, *22*, 20–36, 1983.

Gordon, H. R., D. K. Clark, J. L. Mueller and W. A. Hovis, Phytoplankton pigments derived from the Nimbus–7 CZCS: initial comparisons with surface measurements, *Science*, *210*, 63–66, 1980.

Gordon, H. R. and M. Wang, Surface Roughness Considerations for Atmospheric Correction of Ocean Color Sensors. 2: Error in the Retrieved Water-leaving Radiance, *Applied Optics*, *31*, 4261–4267, 1992a.

Gordon, H. R. and M. Wang, Surface Roughness Considerations for Atmospheric Correction of Ocean Color Sensors. 1: The Rayleigh Scattering Component, *Applied Optics*, *31*, 4247–4260, 1992b.

Gordon, H. R. and M. Wang, Retrieval of water-leaving radiance and aerosol optical thickness over the oceans with SeaWiFS: A preliminary algorithm, *Applied Optics*, *33*, 443–452, 1994a.

Gordon, H. R. and M. Wang, Influence of Oceanic Whitecaps on Atmospheric Correction of SeaWiFS, *Applied Optics*, *33*, 7754–7763, 1994b.

Gordon, H. R. and T. Zhang, 1996, How well can radiance reflected from the ocean-atmosphere system be predicted from measurements at the sea surface?, *Applied Optics* (In press).

Grant, W. B., E. V. Browell, C. F. Butler, M. A. Fenn and G. D. Nowicki, Comparisons of Electra-Lidar and LITE Atmospheric Measurements Near the East Coast of the U.S. and the Caribbean, *EOS, Transactions, American Geophysical Union*, *76*, S70, 1995.

Hale, G. M. and M. R. Querry, Optical Constants of Water in the 200-nm to 200-μm Wavelength Region, *Applied Optics*, *12*, 555–563, 1973.

Holben, B. N., T. F. Eck, I. Slutsker, D. Tanre, J. P. Buis, A. Setzer, E. Vermote, J. Reagan, Y. Kaufman, T. Nakajima, F. Lavenu and I. Jankowiak, 1996, Automatic Sun and Sky Scanning Raiometer System for Network Aerosol Monitoring, *Remote Sensing of Environment* (In press) .

Hooker, S. B., W. E. Esaias, G. C. Feldman, W. W. Gregg and C. R. McClain, *SeaWiFS Technical Report Series: Volume 1, An Overview of SeaWiFS and Ocean Color*, NASA, Greenbelt, MD, Technical Memorandum 104566, July 1992.

Hovis, W. A., D. K. Clark, F. Anderson, R. W. Austin, W. H. Wilson, E. T. Baker, D. Ball, H. R. Gordon, J. L. Mueller, S. Y. E. Sayed, B. Strum, R. C. Wrigley and C. S. Yentsch, Nimbus 7 coastal zone color scanner: system description and initial imagery, *Science*, *210*, 60–63, 1980.

van de Hulst, H. C., *Multiple Light Scattering*, Academic Press, New York, 1980, 739 pp.

Ismail, S., E. V. Browell, S. A. Kooi and G. D. Nowicki, Simultaneous LASE and LITE Aerosol Profile Measurements over the Atlantic, *EOS, Transactions, American Geophysical Union*, *76*, S71, 1995.

Junge, C., Atmospheric Chemistry, *Advances in Geophysics*, *4*, 1–108, 1958.

Kattawar, G. W., G. N. Plass and S. J. Hitzfelder, Multiple scattered radiation emerging from Rayleigh and continental haze layers. 1: Radiance, polarization, and neutral points, *Applied Optics*, *15*, 632–647, 1976.

Kenizys, F. X., E. P. Shettle, W. O. Gallery, J.H.Chetwynd, L. W. Abreu, J. E. A. Selby, S. A. Clough and R. W. Fenn, Atmospheric Transmittance/Radiance: The LOWTRAN 6 Model, Air Force Geophysics Laboratory, Hanscomb AFB, MA 01731, AFGL–TR–83–0187, 1983, NTIS AD A137796.

King, M. D., Harshvardhan and A. Arking, A Model of the Radiative Properties of the El Chichón Stratospheric Aerosol Layer, *Journal of Climate and Applied Meteorology*, *23*, 1121–1137, 1984.

Koepke, P., Vicarious Satellite Calibration in the Solar Spectral Range by Means of Calculated Radiances and its Application to Meteosat, *Applied Optics*, *21*, 2845–2854, 1982.

Koepke, P., Effective Reflectance of Oceanic Whitecaps, *Applied Optics*, *23*, 1816–1824, 1984.

Korotaev, G. K., S. M. Sakerin, A. M. Ignatov, L. L. Stowe and E. P. McClain, Sun-Photometer Observations of Aerosol Optical Thickness over the North Atlantic from a Soviet Research Vessel for Validation of Satellite Measurements, *Jour. Atmos. Oceanic Technol.*, *10*, 725–735, 1993.

Lechner, I. S., G. W. Fisher, H. R. Larsen, M. J. Harvey and R. A. Knobben, Aerosol Size Distributions in the Southwest Pacific, *Jour. Geophys. Res.*, *94D*, 14893–14903, 1989.

McCormick, M. P., LITE – An Overview, *EOS, Transactions, American Geophysical Union*, *76*, S66, 1995.

Mishchenko, M. I. and L. D. Travis, Light scattering by polydispersions of randomly oriented spheriods with sizes comparable to wavelengths of observation, *Applied Optics*, *33*, 7206–7225, 1994.

Morel, A. and J. -M. André, Pigment Distribution and Primary Production in the Western Mediterranean as Derived and Modeled From Coastal Zone Color Scanner Observations, *Jour. Geophys. Res.*, *96C*, 12,685–12,698, 1991.

Morel, A. and B. Gentili, Diffuse reflectance of oceanic waters: its dependence on Sun angle as influenced by the molecular scattering contribution, *Applied Optics*, *30*, 4427–4438, 1991.

Morel, A. and B. Gentili, Diffuse reflectance of oceanic waters. II. Bidirectional aspects, *Applied Optics*, *32*, 6864–6879, 1993.

Morel, A. and B. Gentili, 1996, Diffuse reflectance of oceanic waters. III. Implication of bidirectionality for the remote sensing problem, *Applied Optics* (In press).

Morel, A., K. J. Voss and B. Gentili, Bidirectional reflectance of oceanic waters: A comparison of modeled and measured upward radiance fields, *Jour. Geophys. Res.*, *100C*, 13,143–13,150, 1995.

Mugnai, A. and W. J. Wiscombe, Scattering from nonspherical Chebyshev particles. 3: Variability in angular scattering patterns, *Applied Optics*, *28*, 3061–3073, 1989.

Neckel, H. and D. Labs, The Solar Radiation Between 3300 and 12500 Å, *Solar Physics* , *90*, 205–258, 1984.

Neville, R. A. and J. F. R. Gower, Passive Remote Sensing of Phytoplankton via Chlorophyll α Fluorescence, *Jour. Geophys. Res.*, *82C*, 3487–3493, 1977.

Platt, T. and S. Sathyendranath, Oceanic Primary Production: Estimation by Remote Sensing at Local and Regional Scales, *Science*, *241*, 1613–1620, 1988.

Reddy, P. J., F. W. Kreiner, J. J. Deluisi and Y. Kim, Aerosol Optical Depths Over the Atlantic Derived From Shipboard Sunphotometer Observations During the 1988 Global Change Expedition, *Global Biogeochemical Cycles*, *4*, 225–240, 1990.

Salomonson, V. V., W. L. Barnes, P. W. Maymon, H. E. Montgomery and H. Ostrow, MODIS: Advanced Facility Instrument for Studies of the Earth as a System, *IEEE Geosci. Rem. Sens.*, *27*, 145–152, 1989.

Sasano, Y. and E. V. Browell, Light scattering characteristics of various aerosol types derived from multiple wavelength lidar observations, *Applied Optics*, *28*, 1670–1679, 1989.

Schwindling, M., Modeles et measures pour l'observation spatiale de la couleur de l'ocean: Diffusion atmospherique par les aerosols et reflexion de surface par l'ecume, 1995, Docteur de L'Universite these, Univ. des Sci. et Tech. de Lille. 245 pp.

Shettle, E. P. and R. W. Fenn, Models for the Aerosols of the Lower Atmosphere and the Effects of Humidity Variations on Their Optical Properties, Air Force Geophysics Laboratory, Hanscomb AFB, MA 01731, AFGL–TR–79-0214, 1979.

Slater, P. N., S. F. Biggar, R. G. Holm, R. D. Jackson, Y. Mao, M. S. Moran, J. M. Palmer and B. Yuan, Reflectance- and Radiance-Based Methods for the In-Flight Absolute Calibration of Multispectral Sensors, *Remote Sensing of Environment*, *22*, 11–37, 1987.

Smith, R. C., Structure of Solar Radiation in the Upper Layers of the Sea, in *Optical Aspects of Oceanography*, edited by N. G. Jerlov and E. S. Nielsen, pp. 95–119, Academic Press, New York, NY, 1974.

Smith, R. C. and W. H. Wilson, Ship and satellite bio-optical research in the California Bight, in *Oceanography from Space*, edited by J. F. R. Gower, pp. 281–294, Plenum, New York, NY, 1981.

Tomasi, C., Weak Absorption by Atmospheric Water Vapour in the Visible and Near-Infrared Spectral Region, *Nuovo Cimento*, *2C*, 511–526, 1979a.

Tomasi, C., Non-selective absorption by atmospheric water vapour at visible and near infrared wavelengths, *Quart. J. R. Met. Soc.*, *105*, 1027–1040, 1979b.

Villevalde, Y. V., A. V. Smirnov, N. T. O'Neill, S. P. Smyshlyaev and V. V. Yakovlev, Measurement of Aerosol Optical Depth in the Pacific Ocean and North Atlantic, *Jour. Geophys. Res.*, *99D*, 20983–20988, 1994.

Voss, K. J., Electro-optic Camera System for Measurement of the Underwater Radiance Distribution, *Optical Engineering*, *28*, 241–247, 1989.

Wang, M. and H. R. Gordon, Retrieval of the Columnar Aerosol Phase Function and Single Scattering Albedo from Sky Radiance over the Ocean: Simulations, *Applied Optics*, *32*, 4598–4609, 1993.

Wang, M. and H. R. Gordon, Radiance reflected from the ocean-atmosphere system: Synthesis from individual components of the aerosol size distribution, *Applied Optics*, *33*, 7088–7095, 1994a.

Wang, M. and H. R. Gordon, A Simple, Moderately Accurate, Atmospheric Correction Algorithm for SeaWiFS, *Remote Sensing of Environment*, *50*, 231–239, 1994b.

Wang, M. and H. R. Gordon, Estimating aerosol optical properties over the oceans with the multiangle imaging spectroradiometer: Some preliminary studies, *Applied Optics*, *33*, 4042–4057, 1994c.

Whitlock, C. H., D. S. Bartlett and E. A. Gurganus, Sea Foam Reflectance and Influence on Optimum Wavelength for Remote Sensing of Ocean Aerosols, *Geophys. Res. Lett.*, *7*, 719–722, 1982.